Simulating Hydraulic Fracturing Dynamics Considering Dynamic Biot's Poroelasticity and Coupled Plasticity–Damage Permeability

Shu-Gang Ai[1] and Ke Gao[2]

Abstract: Fluid injection is widely used to enhance permeability in rock formations by creating or dilating transport pathways for resources such as oil, gas, heat, or CO_2. The dynamic propagation of damage induced by fluid injection is governed by fluid flow, dynamic poroelastic deformation, mixed tensile and shear failure, and damage-induced antipermeability degradation. However, the transition from elastoplastic deformation to mixed-mode failure, as well as the induced dynamics, remains ambiguous. This study combines the dynamic Biot's poroelasticity and coupled Drucker–Prager plasticity, Grady–Kipp damage, and antipermeability degradation to simulate dynamic hydraulic fracturing. An explicit predictor–corrector scheme was employed to solve the dynamics of saturated porous media and identify the key factors controlling dynamic damage propagation. The proposed model was tested on soil column consolidation and rock hydraulic fracturing driven by a pre-existing crack, demonstrating good agreement between the numerical and experimental results. Simulation results indicate that damage zones facilitate preferential flow during fluid injection due to damage-induced degradation. The most extensive damage zone is observed under strong damage–permeability coupling. Shear plasticity, tensile damage, and induced seismicity are dominated by fracturing dynamics induced by fluid injection. Oscillations in the temporal–spatial evolution of damaged and plastic points, cumulated potency, and moment magnitude confirm the fracturing dynamics. Shorter injection times result in stronger dynamics and more significant damage propagation. The period of oscillations in cumulated potency increases with injection time while their amplitude gradually decreases due to energy release. These findings highlight injection-induced fracturing dynamics, offering novel insights into the dynamic propagation of damage coupled with matrix antipermeability degradation. **DOI: 10.1061/IJGNAI.GMENG-10274**.

Practical Applications: The insights gained from this study on dynamic hydraulic fracturing have significant practical implications for industries utilizing fluid injection to enhance permeability in rock formations. By understanding the factors controlling dynamic damage propagation, engineers can optimize fluid injection strategies to maximize permeability enhancement while minimizing unintended damage. The findings regarding the influence of injection time on fracturing dynamics can inform the design of injection protocols to control the extent and impact of induced seismicity. Moreover, the study's validation of the proposed model against experimental and numerical results provides a reliable tool for predicting damage zones and preferential flow paths, which can be used in planning and managing fluid injection operations. This research contributes to safer and more efficient extraction of subsurface resources and the effective sequestration of CO_2, ultimately aiding in the advancement of sustainable energy practices and environmental protection.

Author keywords: Fluid injection; Coupled plasticity–damage; Antipermeability degradation; Mixed-mode failure; Fracturing dynamics.

Introduction

Hydraulic fracturing is commonly used to enhance the production of natural gas and oil from shales (Chen et al. 2021; Rahimi-Aghdam et al. 2019), extract geothermal energy from hot dry rock (HDR) reservoirs (AbuAisha et al. 2016; Guo et al. 2023; Kruszewski et al. 2021), and sequestrate captured carbon dioxide (CO_2) into underground geological formations such as deep saline aquifers (Cheng et al. 2022; Raziperchikolaee et al. 2013). This technique injects high-pressure fluid into a wellbore, which may dilate existing fractures or faults around the wellbore or create new fractures in subsurface rocks, with the goal of enhancing permeability in the target rock formation. Despite the widespread use of hydraulic fracturing in various applications, it is crucial to gain a deeper understanding of the underlying dynamics involved in this process for optimizing fracture design and enhancing the efficiency of hydraulic fracturing operations. In dynamic hydraulic fracturing simulations, the stepwise crack tip advancement and pressure oscillations were confirmed (Cao et al. 2018; Peruzzo et al. 2019; Pizzocolo et al. 2013). The fracturing dynamics essentially affect crack initiation and propagation and fracture complexity. To gain insight into these effects, it is necessary to conduct detailed simulations of dynamic hydraulic fracturing induced by fluid injection.

Many studies have sought to simulate hydraulic fracturing in rock formations. Tang et al. (2002) developed a coupled flow–stress–damage (FSD) model for heterogeneous rocks to investigate the hydromechanical coupling process. Shalev and Lyakhovsky

[1]Research Assistant Professor, Dept. of Earth and Space Sciences, Southern Univ. of Science and Technology, Shenzhen 518055, China. ORCID: https://orcid.org/0000-0002-5495-1093. Email: aisg@sustech.edu.cn

[2]Associate Professor, Guangdong Provincial Key Laboratory of Geophysical High-Resolution Imaging Technology, Dept. of Earth and Space Sciences, Southern Univ. of Science and Technology, Shenzhen 518055, China (corresponding author). ORCID: https://orcid.org/0000-0002-0908-7056. Email: gaok@sustech.edu.cn

Note. This manuscript was submitted on February 6, 2024; approved on September 17, 2024; published online on January 17, 2025. Discussion period open until June 17, 2025; separate discussions must be submitted for individual papers. This paper is part of the ***International Journal of Geomechanics***, © ASCE, ISSN 1532-3641.

(2013) studied the processes controlling damage zone propagation induced by fluid injection using a coupled damage rheology and Biot's poroelasticity model. However, the inertia term in the balance equation of the rock matrix in these studies was neglected. Recently, Parchei-Esfahani and Gracie (2019) filled this gap by implementing a fully coupled hydroelastodynamic extended FEM (XFEM) model. Also, Parchei-Esfahani et al. (2020) performed the dynamic simulation of hydraulic fractures induced by fracturing from a wellbore using pressure pulsing. In addition to the internal physical processes mentioned previously, the evaluation of permeability enhancement and dynamic stress drop in rock formations necessitates the consideration of external conditions, such as loading conditions and the initial stress state. Cao et al. (2018) studied the dynamic behavior of fracturing in saturated porous media under different loading conditions, such as fluid injection velocity. Parchei-Esfahani and Gracie (2019) showed that the hydraulically induced fracture trajectories are significantly affected by the direction of pre-existing fracture and the intensity of in situ stress anisotropy. Lyakhovsky and Shalev (2021) considered the pre-existing faults while simulating injection-induced seismicity. Keilegavlen et al. (2021) improved seismic interpretations for understanding injection-induced fault reactivation using a hydromechanical and faulted geothermal reservoir simulation model. Due to the complexity involved, there are only limited studies that consider all aspects of the simulation, including the coupled multiphysical processes and the critical external conditions (Lepillier et al. 2020; Li et al. 2023b; Wang et al. 2009; Zhao and Young 2011). The mechanisms involved in hydraulic fracturing are intricate, probably encompassing fluid injection and flow, dynamic poroelastic deformation, mixed-mode failure composed of plastic shear and tensile damage (resulting in stress drop and seismicity), and damage-induced antipermeability degradation. Incorporating these processes, particularly the mixed tensile-shear fracture considering dynamic effects, is essential to accurately simulate the complete process caused by fluid injection in rocks.

Numerous researchers have pursued the coupled plasticity–damage model to capture shear plasticity and tensile damage using continuum-based methods such as the FEM, smoothed particle hydrodynamics (SPH), and material point method (MPM). Chen (1999) first developed a microcrack-based continuum damage model by coupling Drucker–Prager plasticity and Grady–Kipp damage in the FEM framework to study the nonlocal effects on dynamic damage accumulation in brittle solids. The Grady–Kipp damage model was modified by Das and Cleary (2010), where only the tensile components of stress are reduced due to tensile damage, and the Drucker–Prager plasticity model for shear failure was then coupled within the SPH framework by Pramanik and Deb (2015). Douillet-Grellier et al. (2016) demonstrated the accuracy of the resulting coupled plasticity–damage model by simulating the initiation and propagation of Mode I, Mode II, and mixed-mode failure under uniaxial compression. After this, the coupled Drucker–Prager and modified Grady–Kipp model was incorporated into the MPM framework to simulate the failure of aggregate materials (Raymond et al. 2019) and then the shearing of polycrystalline materials (Raymond et al. 2021). Additionally, some studies have attempted to simulate the hydraulic fracturing process using the continuum-based plasticity–damage model (Chen and Shen 2021; Pan et al. 2016). Therefore, the fluid–solid coupling is modeled by the interfacial interaction between fluid-free surface and solid fracture, which leads to limited application in large-scale engineering due to the extremely high computational cost. The combination of dynamic Biot's poroelasticity and coupled plasticity–damage–permeability should be a reasonable choice for the simulations of hydraulic fracturing induced by fluid injection; however, to the best of our knowledge, there is no evidence that such a multiprocess coupling system has been performed to investigate hydraulic fracturing dynamics in the existing literature.

In this study, we aim to explore the mechanical mechanisms that control the dynamic propagation of damage induced by fluid injection in rock formulations. To achieve this, we employed the modeling and the simulations of coupled multiprocesses that occur during the injection. Specifically, we combined dynamic Biot's poroelasticity and coupled plasticity–damage–permeability to model the hydromechanical coupling. We validated the proposed model through testing in scenarios involving soil column consolidation and rock hydraulic fracturing driven by a pre-existing crack. Furthermore, we examined the factors influencing fluid transport, damage evolution, and induced seismicity propagation, such as the damage–permeability coupling coefficient, the anisotropic in situ stress field, and the loading rate of fluid injection pressure.

Model Formulation

In this section, we first utilize a set of two-phase Biot's equations to model the initiation and propagation of fluid injection-induced damage over time as an evolutionary outcome of the interaction between fluid flow and porous rock matrix deformation (Chan et al. 2022; Lewis and Schrefler 1998; Navas et al. 2022; Parchei-Esfahani et al. 2020). In the modeling, the plasticity–damage constitutive model used for capturing the mixed tensile-shear fracture behavior of the solid phase is coupled to the matrix permeability that may significantly influence the fluid flow in saturated porous media (Douillet-Grellier et al. 2016; Picandet et al. 2001). We then numerically solve the coupled system of nonlinear governing equations using the standard central difference explicit Newmark time integration scheme (Navas et al. 2022). We finally describe the model configurations employed for studying the dynamic propagation of damage induced by fluid injection.

Conservation of Mass and Linear Momentum

Here, we follow the formulation in Lewis and Schrefler (1998) for multiphysics and multiphase flow in a nonisothermal unsaturated porous medium. The porous rock matrix deforms due to the coupling interaction between the fluid, solid, and thermal fields. The macroscopic mass conservation for fluid and solid phases is then given as follows:

$$\left(\frac{\alpha-n}{K_s}S_w^2+\frac{nS_w}{K_w}\right)\frac{\partial p_w}{\partial t}+\left(\frac{\alpha-n}{K_s}S_wS_g\right)\frac{\partial p_g}{\partial t}-\beta_{sw}\frac{\partial T}{\partial t}+\alpha S_w\nabla\cdot v^s$$
$$+\left(\frac{\alpha-n}{K_s}S_wp_w-\frac{\alpha-n}{K_s}S_wp_g+n\right)\frac{\partial S_w}{\partial t}+\frac{1}{\rho_w}\nabla\cdot(nS_w\rho_wv^{ws})=-\frac{\dot{m}_e}{\rho_w} \quad (1)$$

where fluid (usually water) and gas saturations satisfy $S_w+S_g=1$ because the pore volume in the porous medium is fully occupied by water and gas; p_w, p_g, and T = pore-water pressure, gas pressure, and temperature, respectively; $\alpha=1-K_T/K_s$ = Biot's coefficient, which is approximately equal to one in hydromechanical applications as the solid grains are much more rigid than the fluid–solid mixture; K_T, K_s, and K_w = skeleton, solid, and fluid bulk moduli, respectively; n = porosity; $\beta_{mt}=S_w[(\alpha-n)\beta_s+n\beta_w]$ = thermal expansion coefficient of the mixture as a combination of the solid β_s and the fluid β_w; $\dot{m}_e$ = mass rate of water lost through evaporation per unit volume; and $\mathbf{v}^s$ and $\mathbf{v}^{ws}$ = solid velocity and water relative

velocity with respect to the solid, respectively; water, solid, and mixture densities satisfy $\rho = nS_w\rho_w + (1-n)\rho_s$.

Within this study, the following assumptions are made: (1) the fluid–solid mixture is assumed to be fully water saturated; consequently, $S_g = 0$, $S_w = 1$, $\partial S_w/\partial t = 0$, and $\partial p_g/\partial t = 0$; (2) the two-phase media is assumed to be isothermal, which results in $\partial T/\partial t = 0$; (3) the spatial variation of the fluid density is neglected, which leads to $\nabla\rho_w = 0$; and (4) the pore-water phase change including evaporation and condensation is not be considered, i.e., $\dot{m}_e = 0$. Under the aforementioned assumptions, the mass conservation equation [Eq. (1)] can be simplified as follows:

$$\left(\frac{1-n}{K_s} + \frac{n}{K_w}\right)\frac{\partial p_w}{\partial t} + \nabla\cdot v^s + \nabla\cdot(nv^{ws}) = 0 \tag{2}$$

Let $\mathbf{u}$ and $\mathbf{U}$, respectively, denote the displacement of the solid skeleton and the absolute displacement of the fluid such that the relative displacement of the fluid with respect to the solid in the mixture is formulated as $\mathbf{w} = nS_w(\mathbf{U}-\mathbf{u}) = \mathbf{u}^{ws}$. Let $Q = (1-n)/K_s + n/K_w$ denote the volumetric compressibility of the porous mixture, then Eq. (2) can be rewritten as follows (Navas et al. 2022):

$$\frac{\dot{p}_w}{Q} + \nabla\cdot\dot{\mathbf{u}} + \nabla\cdot\dot{\mathbf{w}} = 0 \tag{3}$$

Considering the conservation of linear momentum for the fluid phase, the generalized Darcy law is derived by Lewis and Schrefler (1998), and thus, the Darcy velocity is defined as follows:

$$\dot{\mathbf{w}} = nS_w\mathbf{v}^{ws} = \frac{k^{rw}\mathbf{k}}{\mu_w}[-\nabla p_w + \rho_w(\mathbf{g} - \ddot{\mathbf{u}} - \ddot{\mathbf{w}})] \tag{4}$$

where $\ddot{\mathbf{u}}$ and $\ddot{\mathbf{w}}$ = acceleration of the solid skeleton and the relative acceleration of the fluid phase with respect to the solid phase; $\mathbf{g}$ = gravity acceleration; μ_w = dynamic viscosity of the water; k^{rw} = water relative permeability coefficient (usually equal one); $\mathbf{k}$ = intrinsic permeability tensor of the fluid–solid mixture; and $\mathbf{k} = k\mathbf{I}$ for the case of isotropic permeability in which the intrinsic permeability k is replaced by the hydraulic conductivity κ by $k = \mu_w\kappa/(\rho_w g)$. Substituting Eq. (4) back into Eq. (3) while the fluid acceleration with respect to the solid is disregarded (i.e., $\ddot{\mathbf{w}} = 0$) (Cao et al. 2018), the mass balance equation for the isothermal fully saturated porous medium is obtained as follows:

$$\dot{p}_w = -Q\nabla\cdot\dot{\mathbf{u}} + Q\frac{k\mathbf{I}}{\mu_w}\nabla\cdot(\rho_w\mathbf{g} - \rho_w\ddot{\mathbf{u}} - \nabla p_w) \tag{5}$$

In addition, the linear momentum balance equation for the solid phase can be expressed as follows:

$$\nabla\cdot(\boldsymbol{\sigma}' - p_w\mathbf{I}) - \rho\ddot{\mathbf{u}} + \rho\mathbf{g} = \mathbf{0} \tag{6}$$

where $\boldsymbol{\sigma}'$ = effective stress tensor and is defined as $\boldsymbol{\sigma}' = \boldsymbol{\sigma} + p_w\mathbf{I}$ based on Terzaghi's effective stress theory, which is negative in compression other than the pore fluid pressure in this study. To sum up, Eqs. (5) and (6) represent the final $\mathbf{u} - p_w$ formulation involving two primary unknowns (i.e., the solid displacement and pore fluid pressure) for dynamic saturated flow problems in a porous medium.

Coupling between Plasticity–Damage and Permeability

We employed the continuum plasticity-damage model proposed by Douillet-Grellier et al. (2016) to account for mixed tensile–shear failure in an FEM framework. In this section, we describe sequentially the constitutive theory and implementation of the classical Drucker–Prager model for plastic shear failure and the Grady–Kipp damage model for tensile failure. The implementation includes elastic prediction, plastic correction, and damage calculation. This is then followed by a description of the coupling between plasticity–damage and permeability in the dynamic hydromechanical regime.

First, we consider the case of plane strain deformation for the porous medium. Hence, the yield surface of the Drucker–Prager model usually passes through the inner apexes of the Mohr–Coulomb model in the π-plane. Under the trial elastic stress state, it is formulated as follows:

$$\begin{cases} \Phi_{n+1}^{\text{trial}} = \|\mathbf{s}_{n+1}^{\text{trial}}\| + 3\alpha_F p_{n+1}^{\text{trial}} - \beta c_n \\ \alpha_F = \sqrt{2\tan^2\phi/(9+12\tan^2\phi)} \\ \alpha_Q = \sqrt{2\tan^2\psi/(9+12\tan^2\psi)} \\ \beta_C = \sqrt{18/(9+12\tan^2\phi)} \end{cases} \tag{7}$$

where $\mathbf{s}_{n+1}^{\text{trial}}$ and p_{n+1}^{trial} = trial deviatoric and volumetric stresses at the time step $n+1$, respectively; α_F, α_Q, and β_C = constitutive parameters; c_n = cohesion or tensile strength related to the plastic state; and ϕ and ψ = internal friction and dilatancy angles, respectively. The resulting trial yield function $\Phi_{n+1}^{\text{trial}}$ determines the real stress state at the current time step $n+1$. When $\Phi_{n+1}^{\text{trial}} > 0$, the material is under plastic deformation and plastic correction is required. Since the yield surface of the Drucker–Prager model is nonsmooth as a circular cone and usually divided into the smooth and apex portions, consequently resulting in the corresponding two return mapping algorithms, it behooves us to decide in advance which algorithm to employ according to the trial stress before the plastic return procedure. The critical value of the volumetric stress $p_{n+1}^{\text{trial(limit)}}$ provided by Navas et al. (2022) precisely works, which is given as follows:

$$\begin{cases} p_{n+1}^{\text{trial(limit)}} = \dfrac{3\alpha_Q K}{2G}\|\mathbf{s}_{n+1}^{\text{trial}}\| + \dfrac{\beta_C}{3\alpha_F}\left(\dfrac{\|\mathbf{s}_{n+1}^{\text{trial}}\|}{2G}H_n\sqrt{1+3\alpha_Q^2} + c_n\right) \\ c_n = c_0(1-\bar{\varepsilon}_n^p/\varepsilon_0)^{1/N^\epsilon}, \quad H_n = \dfrac{\partial c_n}{\partial\bar{\varepsilon}^p} = \dfrac{c_0}{N^\epsilon\varepsilon_0}(1-\bar{\varepsilon}_n^p/\varepsilon_0)^{(1/N^\epsilon-1)} \end{cases} \tag{8}$$

where K and G = bulk and shear moduli of the material, respectively; c_0 = initial tensile strength that reduces based on the aforedefined exponential softening law (Camacho and Ortiz 1997) when plastic deformation measured by the equivalent plastic strain $\bar{\varepsilon}_n^p$ begins; ε_0 = reference plastic strain; H_n = generalized hardening modulus similarly related to the plastic state; and N^ϵ = softening exponent that is taken as one in this study. When $p_{n+1}^{\text{trial}} \le p_{n+1}^{\text{trial(limit)}}$, the return to the smooth portion algorithm is performed to fulfill the consistency requirement (i.e., $\Phi_{n+1}^{\text{smooth}} = 0$). The same goes for the case of returning to the apex. The nonlinear yield functions for the two cases are given as follows (Sanavia et al. 2006):

$$\begin{cases} \Phi_{n+1}^{\text{smooth}} = \|\mathbf{s}_{n+1}^{\text{trial}}\| - 2G\Delta\gamma_{n+1} + 3\alpha_F(p_{n+1}^{\text{trial}} - 3\alpha_Q K\Delta\gamma_{n+1}) - \beta_C c_{n+1} \\ \Phi_{n+1}^{\text{apex}} = \dfrac{\beta_C}{3\alpha_F}\left[c_n + H_n\sqrt{(\Delta\gamma_{n+1}^{(1)})^2 + 3\alpha_Q^2(\Delta\gamma_{n+1}^{(1)} + \Delta\gamma_{n+1}^{(2)})^2}\right] \\ \quad -p_{n+1}^{\text{trial}} + 3\alpha_Q K(\Delta\gamma_{n+1}^{(1)} + \Delta\gamma_{n+1}^{(2)}) \end{cases} \tag{9}$$

where $\Delta\gamma_{n+1}$ = plastic multiplier using the Newton–Raphson method for the smooth returning; and $\Delta\gamma_{n+1}^{(1)}$ and $\Delta\gamma_{n+1}^{(2)}$ = plastic multipliers for the apex returning; and $\Delta\gamma_{n+1}^{(1)} = \|\mathbf{s}_{n+1}^{\text{trial}}\|/(2G)$. Such an iterative solution process successfully brings the current stress back to the Drucker–Prager yield surface. At the end of the implicit stress integration procedure, the following plastic

Int. J. Geomech., 2025, 25(4): 04025019

correction has to be carried out:

$$\begin{cases} \bar{\varepsilon}_{n+1}^{p(smooth)} = \bar{\varepsilon}_{n}^{p(smooth)} + \Delta\gamma_{n+1}\sqrt{3\alpha_{\mathrm{Q}}^2 + 1} \\ \bar{\varepsilon}_{n+1}^{p(apex)} = \bar{\varepsilon}_{n}^{p(apex)} + \sqrt{\left(\Delta\gamma_{n+1}^{(1)}\right)^2 + 3\alpha_{\mathrm{Q}}^2\left(\Delta\gamma_{n+1}^{(1)} + \Delta\gamma_{n+1}^{(2)}\right)^2} \end{cases} \tag{10}$$

We also consider the tensile failure of the solid, in addition to the plastic shear failure described, as a damage evolution using the Grady–Kipp model (Douillet-Grellier et al. 2016; Grady and Kipp 1980; Raymond et al. 2019, 2021). After the previous elasto-plastic calculation, we next evaluate whether the solid at the updated stress state is under tensile damage using the following strain-based model formulated as follows:

$$\begin{cases} \Phi^{\mathrm{damage}} = \bar{\varepsilon}_{\mathrm{eff}}^{\mathrm{tensile}} - \varepsilon_0^{\mathrm{damage}} \\ \bar{\varepsilon}_{\mathrm{eff}}^{\mathrm{tensile}} = \tilde{\sigma}_{\mathrm{max}}^{\mathrm{tensile}}/(K + 4G/3) \\ \varepsilon_0^{\mathrm{damage}} = (V_{gp}k_{wb})^{-1/m_{wb}} \end{cases} \tag{11}$$

where $\bar{\varepsilon}_{\mathrm{eff}}^{\mathrm{tensile}}$ and $\varepsilon_0^{\mathrm{damage}}$ = effective tensile strain and its initial value, respectively; $\tilde{\sigma}_{\mathrm{max}}^{\mathrm{tensile}}$ = maximum principal stress under tension; V_{gp} = volume of the material point (e.g., Gauss point in FEM); and m_{wb} and k_{wb} = Weibull's parameters controlling the failure or damage activation. When $\Phi^{\mathrm{damage}} > 0$, the tensile damage begins in the solid; at this point, damage calculation and tensile correction are required, which is performed by

$$\begin{cases} \tilde{\sigma}_{i(n+1)}^{\mathrm{tensile}} = (1 - D)\tilde{\sigma}_{i(n)}^{\mathrm{tensile}} \\ \dfrac{dD^{1/3}}{dt} = \dfrac{1}{3}c_g\alpha_{wb}^{1/3}\left(\bar{\varepsilon}_{\mathrm{eff}}^{\mathrm{tensile}}\right)^{1/3} \\ \alpha_{wb} = \dfrac{8\pi k_{wb}(m_{wb} + 3)^2}{(m_{wb} + 1)(m_{wb} + 2)} \end{cases} \tag{12}$$

where $\tilde{\sigma}_i^{\mathrm{tensile}}$ = principal stress under tension satisfying $\tilde{\sigma}_i^{\mathrm{tensile}} \in [\sigma_1, \sigma_2, \sigma_3]$ and $\tilde{\sigma}_i^{\mathrm{tensile}} \geq 0$; c_g = crack growth speed during dynamic failure and is usually regarded as 0.4 times the speed of sound in the solid; and D = damage parameter between zero and one. When $D = 1$, tensile failure occurs, resulting in a zero tensile stress state (i.e., $\tilde{\sigma}_{i(n+1)}^{\mathrm{tensile}} = 0$). In the tensile correction procedure, we first correct the tensile component of the principal stress tensor using D and then rotate the updated principal stress tensor back to the original coordinate frame to form the final total stress considering the strain damage.

A physical fact is revealed by experimental results from previous works (Picandet et al. 2001; Souley et al. 2001; Suzuki et al. 1998) that permeability in the fluid–solid porous medium has a strong connection with material tensile damage. In this study, we adopted the approach proposed by Shalev and Lyakhovsky (2013) for modeling the degradation of matrix antipermeability caused by damage in hydraulic fracturing simulations. We assumed that this degradation depends exponentially on the tensile damage described in this study, which is consistent with the formulation presented in previous studies (Lyakhovsky and Shalev 2021; Picandet et al. 2001; Shalev and Lyakhovsky 2013) and formulated as follows:

$$k(D) = k_0 \exp(bD) \tag{13}$$

where k_0 = porous medium's initial permeability; and b = damage–permeability coupling coefficient. As a result of such coupling, it is possible to simulate dynamic damage propagation induced by fluid injection in the fluid–solid porous medium. This corresponds to the case where a wellbore is pressurized at a high level through fluid injection up to the initiation of tensile damage in the solid, subsequently resulting in a significant reduction of current permeability, concomitantly where the fluid flows rapidly through the damage zone. The high pore pressure therein promotes the further propagation of damage or failure zone. Such hydromechanical coupling mechanisms are investigated using the proposed model in the latter section.

Time-Spatial Discretization and Numerical Solution

The system of nonlinear partial differential equations governing the two-phase fluid–solid coupling in the porous medium was spatially discretized using FEM and solved by the predictor–corrector time integration scheme algorithm based on the Newmark central difference explicit scheme. This scheme has advantages in computational stability and convenience (Liu 1994). The explicit solution procedure was divided into two primary steps: we first calculated the nodal displacements, pore pressures, and velocities at the time step $n+\chi$ according to the already obtained quantities [i.e., $\mathbf{u}_n$, $\dot{\mathbf{u}}_n$, $\ddot{\mathbf{u}}_n$, $p_{w(n)}$, and $\dot{p}_{w(n)}$] at time step n, referred to as the predictor step; we then updated them to reach time step $n+1$ with the nodal accelerations $\ddot{\mathbf{u}}_{n+1}$ and pore pressure rates $\dot{p}_{w(n+1)}$ to be solved, referred to as the corrector step. The predictor–corrector solution for dynamic flow problems is thus formulated as follows:

$$\begin{cases} \dot{\mathbf{u}}_{n+1} = \underbrace{\dot{\mathbf{u}}_n + (1 - \gamma_N)\ddot{\mathbf{u}}_n\Delta t}_{\text{Predictor } \dot{\mathbf{u}}_{n+\chi}} + \underbrace{\gamma_N\ddot{\mathbf{u}}_{n+1}\Delta t}_{\text{Corrector}} \\ \mathbf{u}_{n+1} = \underbrace{\mathbf{u}_n + \dot{\mathbf{u}}_n\Delta t + (0.5 - \beta_N)\ddot{\mathbf{u}}_n\Delta t^2}_{\text{Predictor } \mathbf{u}_{n+\chi}} + \underbrace{\beta_N\ddot{\mathbf{u}}_{n+1}\Delta t^2}_{\text{Corrector}} \\ p_{w(n+1)} = \underbrace{p_{w(n)} + (1 - \theta_N)\dot{p}_{w(n)}\Delta t}_{\text{Predictor } p_{w(n+\chi)}} + \underbrace{\theta_N\dot{p}_{w(n+1)}\Delta t}_{\text{Corrector}} \end{cases} \tag{14}$$

where γ_N, β_N, and θ_N = Newmark parameters ($\gamma_N = \theta_N = 0.5$ and $\beta_N = 0$ in this study); and Δt = time step determined by the Courant–Friedrichs–Lewy condition to be satisfied, i.e.,

$$\Delta t \leq \frac{h_{\min}}{v_c}, \quad v_c = \sqrt{\left(K + \frac{4}{3}G + \frac{K_w}{n_0}\right)\frac{1}{\rho_0}} \tag{15}$$

where n_0 and ρ_0 = initial porosity and density of the mixture, respectively; v_c = P-wave velocity; and $h_{\min}$ = minimum mesh size.

The described predictor step was first performed, and then the resulting incremental nodal displacements $\Delta\mathbf{u}_{n+\chi}$ were used to calculate nodal positions $\mathbf{x}_{n+\chi}$ and incremental deformation gradients at $\Delta\mathbf{F}_{n+\chi}$ Gauss points. The implementation of what follows is to update the deformation gradients $\mathbf{F}_{n+\chi}$, Jacobians $J_{n+\chi}$ and volumes $V_{gp(n+\chi)}$ of Gauss points, and the porosity $n_{n+\chi}$ and density $\rho_{n+\chi}$ of the mixture, which is based on the following equations:

$$\begin{cases} \mathbf{x}_{n+\chi} = \mathbf{x}_n + \Delta\mathbf{u}_{n+\chi}, \ \Delta\mathbf{F}_{n+\chi} = \mathbf{I} + \sum_{nd=1}^{n_{nd}} \Delta\mathbf{u}_{nd(n+\chi)} \otimes \nabla N_{nd} \\ \mathbf{F}_{n+\chi} = \Delta\mathbf{F}_{n+\chi}\mathbf{F}_n, \ J_{n+\chi} = \det\mathbf{F}_{n+\chi}, \ V_{gp(n+\chi)} = J_{n+\chi}V_0 \\ n_{n+\chi} = 1 - \dfrac{1 - n_0}{J_{n+\chi}}, \ \rho_{n+\chi} = n_{n+\chi}\rho_w + (1 - n_{n+\chi})\rho_s \end{cases} \tag{16}$$

where n_{nd} = number of nodes (e.g., all the nodes in a finite element in this study) related to the Gauss point; and ∇N = gradient of the shape function. Based on the elastic logarithmic strain ε_n^e from the previously converged configuration and the deformation gradient increment $\Delta\mathbf{F}_{n+\chi}$, the calculation of the trial elastic logarithmic strain $\boldsymbol{\varepsilon}_{n+\chi}^{e\,\mathrm{trial}}$ follows

$$\mathbf{b}_n^e = \exp(2\boldsymbol{\varepsilon}_n^e), \ \mathbf{b}_{n+\chi}^{e\,\mathrm{trial}} = \Delta\mathbf{F}_{n+\chi}\mathbf{b}_n^e(\Delta\mathbf{F}_n)^T, \ \varepsilon_{n+\chi}^{e\,\mathrm{trial}} = \frac{1}{2}\log\mathbf{b}_{n+\chi}^{e\,\mathrm{trial}} \tag{17}$$

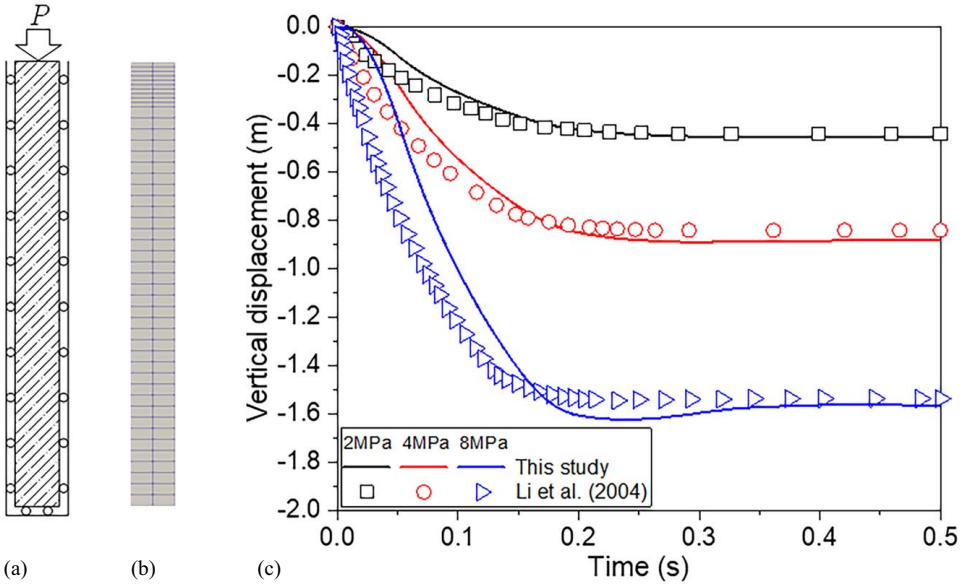

Fig. 1. (a) Geometry and boundary conditions of the soil column; (b) mesh configuration; and (c) comparison of vertical displacement versus time curves from this study and Li et al. (2004).

where $\mathbf{b}_{n+\chi}^{e\ \mathrm{trial}}$ = trial elastic left Cauchy–Green strain matrix. Subsequently, the trial elastic strain was used as the input of constitutive calculation, which permits us to employ the standard small strain Drucker–Prager algorithm [evolving Eqs. (7)–(10)] in the updated Lagrangian large strain FEM. Then, we performed the tensile damage using Eqs. (11) and (12), and update the damage-related matrix permeability $k_{n+\chi}$ using Eq. (13). Also, we calculated the internal forces ($\mathbf{R}_{n+\chi}^{s}$, $\mathbf{R}_{n+\chi}^{pw}$, and $\mathbf{R}_{n+\chi}^{w}$), the external forces [$\mathbf{f}_{n+\chi}^{s(\mathrm{ext})}$ and $\mathbf{f}_{n+\chi}^{w(\mathrm{ext})}$], and the lumped mass and damping matrices ($\mathbf{M}_{n+\chi}^{s}$, $\mathbf{M}_{n+\chi}^{w}$ and $\mathbf{C}_{n+\chi}^{w}$) for the solid and fluid, respectively, which are formulated as follows:

$$\begin{cases} \mathbf{R}_{n+\chi}^{s}=\sum_{gp=1}^{n_{gp}} V_{gp(n+\chi)}\boldsymbol{\sigma}'_{n+\chi}\nabla\mathbf{N}, \quad \mathbf{R}_{n+\chi}^{pw}=\sum_{gp=1}^{n_{gp}} V_{gp(n+\chi)}p_{w(n+\chi)}\nabla\mathbf{N}, \mathbf{R}_{n+\chi}^{w}=\sum_{gp=1}^{n_{gp}} QV_{gp(n+\chi)}\dfrac{k_{n+\chi}}{\mu_w}p_{w(n+\chi)}\nabla\mathbf{N} \\ \mathbf{M}_{n+\chi}^{s}=\sum_{gp=1}^{n_{gp}} V_{gp(n+\chi)}\rho_{n+\chi}\mathbf{N}, \quad \mathbf{C}_{n+\chi}^{w}=\sum_{gp=1}^{n_{gp}} QV_{gp(n+\chi)}\mathbf{BmN}, \quad \mathbf{M}_{n+\chi}^{w}=\sum_{gp=1}^{n_{gp}} QV_{gp(n+\chi)}\dfrac{k_{n+\chi}}{\mu_w}\rho_w\mathbf{BmN} \\ \mathbf{f}_{n+\chi}^{s(\mathrm{ext})}=\mathbf{M}_{n+\chi}^{s}\mathbf{g}-\int_{\partial\Omega_\tau}\boldsymbol{\sigma}'^{\mathrm{ext}}_{n+1}\mathbf{nN}d\Gamma, \quad \mathbf{f}_{n+\chi}^{w(\mathrm{ext})}=\mathbf{M}_{n+\chi}^{w}\mathbf{g}+\int_{\partial\Omega_{pw}}p_{w(n+1)}^{\mathrm{Injection}}\mathbf{nN}d\Gamma \end{cases} \tag{18}$$

where n_{gp} = number of Gauss points; $\boldsymbol{\sigma}'_{n+\chi}$ = updated effective stress; $\mathbf{N}$ and $\mathbf{B}$ = shape function matrix and the symmetric shape function gradient operator, respectively; $\mathbf{m}$ and $\mathbf{n}$ = identity matrix in Voigt notation and the normal vector on the applied boundary surface, respectively; and $\boldsymbol{\sigma}'^{\mathrm{ext}}_{n+1}$ and $p_{w(n+1)}^{\mathrm{Injection}}$ = external pressure and the fluid injection pressure, respectively. Based on the quantities obtained previously, Eqs. (5) and (6) governing the conversation of mass and linear momentum for the fluid–solid mixture are reformulated as follows:

$$\begin{cases} \mathbf{R}_{n+\chi}^{s}-\mathbf{R}_{n+\chi}^{pw}-\mathbf{M}_{n+\chi}^{s}\ddot{\mathbf{u}}_{n+1}+\mathbf{f}_{n+\chi}^{s(\mathrm{ext})}=\mathbf{0} \\ \mathbf{M}_{n+\chi}^{w}\ddot{\mathbf{u}}_{n+1}-\mathbf{C}_{n+\chi}^{w}\dot{\mathbf{u}}_{n+1}+\mathbf{f}_{n+\chi}^{w(\mathrm{ext})}-\mathbf{R}_{n+\chi}^{w}=\dot{p}_{w(n+1)} \end{cases} \tag{19}$$

Numerical Implementation

To reach the system of coupled hydromechanical equations, the explicit solution strategy proposed by Navas et al. (2022) is introduced where the current acceleration $\ddot{\mathbf{u}}_{n+1}$ is first solved by the first equation in Eq. (19), which is subsequently substituted into the first two equations in Eq. (14) for updating the velocity $\dot{\mathbf{u}}_{n+1}$ and the displacement $\mathbf{u}_{n+1}$; the current pore pressure rate $\dot{p}_{w(n+1)}$ is then obtained by substituting the updated quantities into the second equation in Eq. (19), which is used to update the current pore pressure $p_{w(n+1)}$ according to the third equation in Eq. (14). The predictor step is successfully performed in the implementation of the solution strategy. On the premise of the explicit predictor–corrector solution for two-phase fluid–solid coupling problems, our primary goal in what follows is to simulate dynamic hydraulic fracturing induced by fluid injection utilizing damage-induced antipermeability degradation as a fluid flow-driven fracture propagation mechanism.

Model Validation and Discussion

To demonstrate the effectiveness of the proposed model, two cases are presented. First, the soil column consolidation problem is

utilized to assess the capture of Biot's poroelasticity using the explicit predictor–corrector solution. Second, the rock hydraulic fracturing problem driven by a pre-existing crack is examined to illustrate the model's ability to simulate dynamic crack propagation. Finally, the features of the proposed model are discussed.

Soil Column Consolidation

This section compares the consolidation simulation results obtained using the proposed model in this study with those obtained using the method by Li et al. (2004). Fig. 1(a) illustrates the geometry and boundary conditions of the soil column under plane strain assumption. In this case, the soil column is 10 m high and 1 m wide, with horizontal constraints on both sides, a vertical constraint at the bottom, and a free boundary at the top. Fig. 1(b) shows the mesh configuration, which uses four-node linear elements with mesh refinement in the region 1 m below the top surface. This discretization, similar to the approach proposed by Sabetamal et al. (2016), who designed a mesh capable of accurately capturing load-induced waves, has also been adopted by Navas et al. (2022). The material parameters for the soil are taken from Li et al. (2004): the Lamé constants for the solid matrix are $\lambda = 29$ MPa and $\mu = 7$ MPa; the mass densities of the solid and fluid are $\rho_s = 2{,}700$ kg/m^3 and $\rho_w = 1{,}000$ kg/m^3; the porosity is $n = 0.42$; the bulk moduli of the solid and fluid are $K_s = 1.0 \times 10^{34}$ MPa and $K_w = 2.2 \times 10^4$ MPa; and the hydraulic conductivity is $\kappa = 0.1$ m/s. The model proposed in this study is simplified to consider only Neo-Hookean elasticity. During the simulation, a load is applied to the top surface, increasing linearly to its maximum value ($P = 2$, 4, and 8 MPa) within 0.05 s, and then held constant until the total simulation time of 0.5 s is reached. The time step used in the simulation is 1.0×10^{-5} s. Fig. 1(c) shows the vertical displacement at the top surface of the soil column over time. It can be seen that the final steady-state values obtained in this study align closely with those reported by Li et al. (2004) for three different external load conditions. Unlike the quasi-static implicit solution used by Li et al. (2004), this study employs an explicit predictor–corrector method. Consequently, the external load needs to be applied linearly during the initial stage. Additionally, this study captures the dynamic behavior of Biot's poroelasticity. This leads to differences in vertical displacement during the nonsteady-state stage between the two methods.

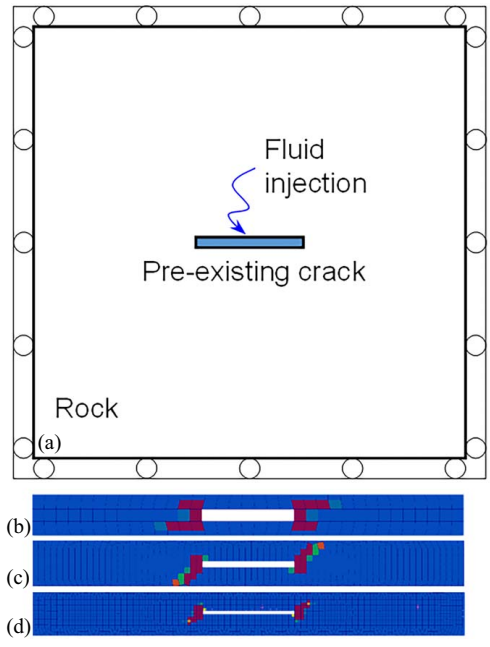

Fig. 2. (a) Geometry and boundary conditions of the rock domain with a pre-existing crack; and (b–d) simulation results obtained using coarse, medium, and fine meshes.

Rock Hydraulic Fracturing

To validate the proposed model in this study, we tested a rock hydraulic fracturing problem driven by a pre-existing crack. Fig. 2(a) presents the geometry and boundary conditions of the rock domain based on the experiments by Liu et al. (2018). In this case, the rock domain measures 0.0707 m × 0.0707 m, featuring a centrally positioned, horizontally oriented pre-existing crack measuring 0.015 mm in length. The boundaries of the domain are fixed in the vertical direction. The fluid pressure increases linearly to 30 MPa within 5×10^{-5} s and then remains constant until 1.0×10^{-4} s. The simulation was conducted with a loading time step of 1.0×10^{-7} s and utilized three different mesh resolutions. Additional parameters utilized in this simulation are detailed in Table 1. Upon comparing simulated results with the experimental findings of Liu et al. (2018), we observed a close correspondence in the initiation location and propagation direction of cracks during the hydraulic fracturing process [Figs. 2(b–d)]. With mesh refinement, the numerical results progressively align more closely with physical observations. Additionally, we noted that mesh resolution influences the extent of crack propagation, with smaller mesh resolutions resulting in larger crack propagation areas. This phenomenon arises from the larger spatial occupancy of cells in grids with smaller resolutions. When damage occurs in these cells, fluid rapidly enters, allowing it to reach areas further from the pre-existing crack.

Model Discussion

Currently, successful modeling of the nucleation and propagation of damage zones resulting from fluid injection in hydrocarbon and geothermal reservoirs has been achieved by coupling various multiphysical processes (Shalev and Lyakhovsky 2013). These

Table 1. Model parameters and initial conditions of the damage–permeability coupling problem

Description	Value
Young's modulus, E (GPa)	30
Poisson's ratio, ν	0.2
Mass density of the solid, ρ_s (kg/m^3)	2,600
Mass density of the water, ρ_w (kg/m^3)	1,000
Bulk modulus of the solid, K_s (MPa)	1.0×10^{34}
Bulk modulus of the water, K_w (MPa)	2.2×10^3
Friction angle, ϕ (°)	38.66
Dilatancy angle, ψ (°)	9.66
Initial cohesion or tensile strength, c_0 (MPa)	5.0
Reference plastic strain, ε_0	0.002
Initial porosity, n_0	0.2
Initial permeability, k_0 (m^2)	2.0×10^{-15}
Damage–permeability coupling coefficient, b	0/14/16
Initial pore pressure, P_{w0} (MPa)	30
Injected fluid overpressure, $P_{w1}^{\text{Injection}}$ (MPa)	45
Fluid injection duration, t_0 (ms)	1.5/2.5/10
Total loading duration, t_1 (ms)	25
Maximum horizontal stress, σ_H (MPa)	−40/−60/−70
Minimum horizontal stress, σ_h (MPa)	−40
Vertical stress, σ_v (MPa)	−55

Note: One or more values used in the simulations in this study are given.

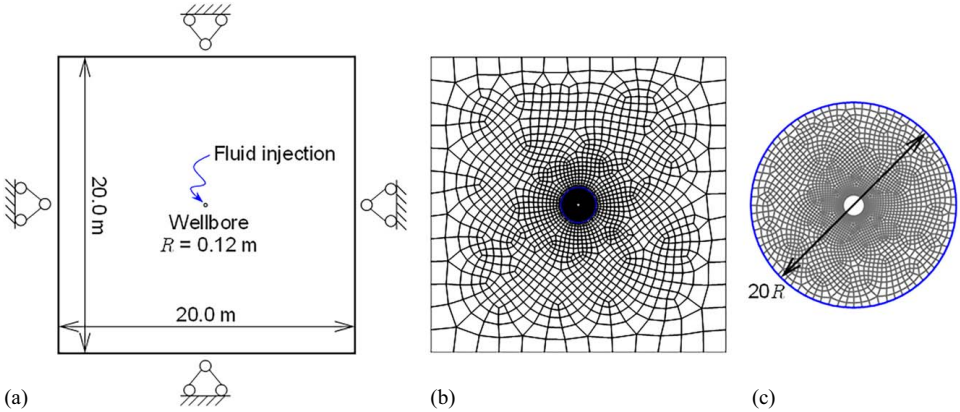

Fig. 3. (a) Schematic initial model configuration for plane strain calculations; (b) unstructured mesh for the global domain; and (c) refined mesh for the local domain near the wellbore. Fluid is injected at the center of the domain into the wellbore with a radius $R = 0.12$ m.

include Biot's poroelastic deformation, generalized Darcy flow, damage rheology (Lyakhovsky et al. 1997), and antipermeability degradation (Picandet et al. 2001; Shalev and Lyakhovsky 2013). The effectiveness and practicality of this model have been confirmed through the simulations of stable and unstable propagation of the damage zones (Lyakhovsky and Shalev 2021; Shalev and Lyakhovsky 2013). However, it is important to note that this study does not primarily focus on damage rheology. Instead, our research aims to elucidate the transition from elastoplastic deformation to mixed tensile–shear fracturing. Additionally, we explore the induced dynamics within the hydraulic fracturing process. Both the transition and the induced dynamics remain ambiguous.

Recently, some scholars have proposed the combination of the elastoplastic model with the cohesive zone model (Liao et al. 2024; Wu et al. 2023; Zhang et al. 2024), which represents an advanced approach for simulating hydraulic fracturing processes while considering plasticity effects. This method offers advantages in simulating complex crack propagation in large-scale fields. However, in this method, the elastoplastic model is only applicable to solid matrix elements, whereas the cohesive zone model is specifically designed for cohesive elements. Consequently, in hydraulic fracturing simulations, a competitive mechanism arises between the elastoplastic deformation of solid elements and the damage and rupture of cohesive elements. As a result, such methods may not adequately capture the transition from elastoplastic deformation to mixed tensile–shear fracturing. Moreover, the time discontinuity issue arises in the numerical implementation of the cohesive zone model, which remains challenging (Maeda et al. 2024; Papoulia et al. 2003).

Based on the previous consideration, this study employed the coupled Drucker–Prager plasticity and Grady–Kipp damage model, which can accurately capture the transition from elastoplastic deformation to damage propagation induced by fluid injection. Validation of the model has been conducted by Douillet-Grellier et al. (2016), Raymond et al. (2019), and Ai and Gao (2023), encompassing uniaxial compression tests, Brazil tests, and tunnel surface spalling tests. Furthermore, the effectiveness of the proposed model is confirmed through the integration of tests on soil column consolidation and rock hydraulic fracturing problems. Therefore, the proposed model in this study can effectively explore the mechanical mechanisms controlling the dynamic propagation of damage induced by fluid injection. In the subsequent sections, we conduct detailed simulations of wellbore hydraulic fracturing, taking dynamic effects into account.

Simulation Results

Model Configuration of Wellbore Fluid Injection

The numerical models are designed to study the dynamic propagation of damage owing to fluid flow in a saturated porous media subjected to wellbore fluid injection. For 2D plane strain calculations, we considered a sandstone reservoir with a physical domain of dimensions [0, 20 m] × [0, 20 m] [Fig. 3(a)]. All outer boundaries are assigned with fixed zero displacements based on the fact that the deformed region in the simulations of dynamic hydraulic fracturing is far from the boundaries. Initial pore-water pressure P_{w0} and anisotropic in situ stress field consisting of maximum horizontal stress σ_H, minimum horizontal stress σ_h, and vertical stress σ_v are simultaneously assigned for the entire domain. A wellbore with a radius $R = 0.12$ m is predrilled at the center of the domain to inject external fluid. Fluid overpressure $P_{w1}^{\text{Injection}}$ above P_{w0} is imposed along the resulting inner wellbore boundary. The loading of the simulation is divided into two stages: linearly increasing pressure loading within t_0 and constant pressure loading from t_0 to t_1 (Fig. 4). Before simulations, the domain is discretized using an unstructured mesh of linear quadrilateral elements where three mesh sizes (i.e., 1.6 m at the outer boundaries, 0.1 m at the near-wellbore circle with a radius of $10R$, and 0.01 m at the wellbore boundary) are employed [Fig. 3(b)], and the element size varies between them. To mitigate the potential impact of mesh dependency, particularly in areas of focused research or concern, the mesh undergoes refinement to ensure physical fidelity. This discretization approach is inspired by Parchei-Esfahani et al. (2020). Subsequently, the final domain is divided into the near-wellbore region discretized by

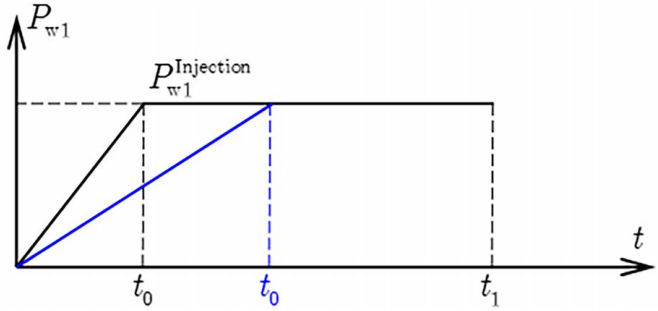

Fig. 4. Injected pressure–time curve of the wellbore fluid.

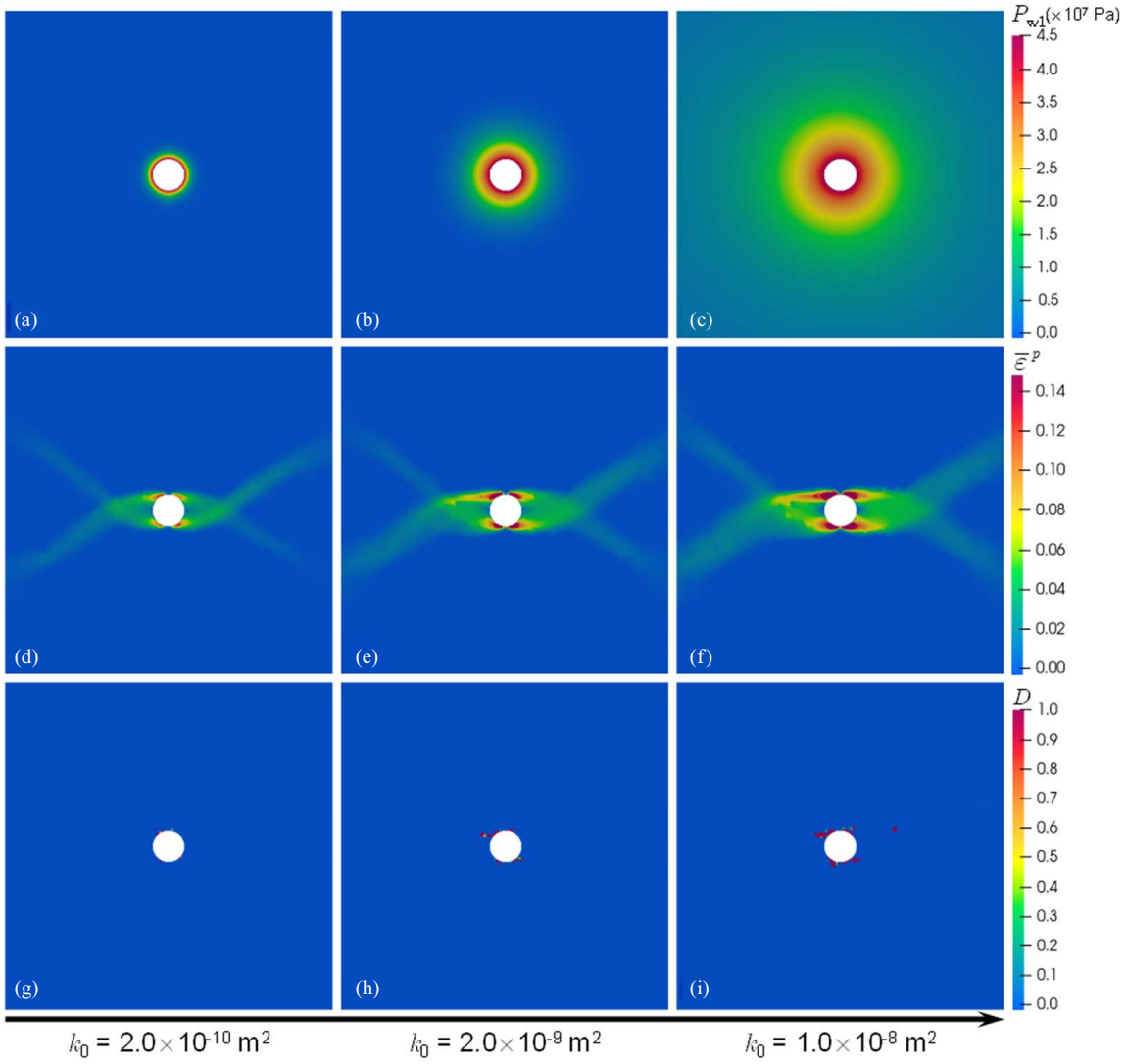

Fig. 5. Comparison of final results for near-wellbore rock formation across three initial intrinsic permeabilities (i.e., $k_0 = 2.0 \times 10^{-10}$, 2.0×10^{-9}, and 1.0×10^{-8} m^2). The coupling between damage and permeability is not considered in all simulations. Examination of three responses after the complete loading: (a–c) overpressure P_{w1}; (d–f) equivalent plastic strain $\bar{\varepsilon}_n^p$; and (g–i) damage D. Note that the 1.25 m × 1.25 m area surrounding the wellbore is extracted as it contains the most notable responses.

finer mesh [Fig. 3(c)] and the rest far-field region. The main parameters used in this study are summarized in Table 1. Additional parameters related to the Grady–Kipp damage model include Weibull's parameter $k_{wb} = 5.39 \times 10^{36}$ and $m_{wb} = 9.0$. The time step is set to 2.5×10^{-6} s in all simulation calculations.

Three key factors controlling the damage dynamic propagation behavior of sandstone reservoirs under fluid injection are considered, and the resulting simulation scenarios are tested in this study. The factors are as follows: (1) the damage–permeability coupling coefficient b in Eq. (13) since the damage-induced variation of matrix permeability increases with the value of b; noteworthily, the permeability is unaffected by the damage when $b = 0$; (2) the anisotropic in situ stress field in the model initial conditions since the initiation and propagation of the damage in the sandstone reservoir depend on the intensity of in situ stress anisotropy; and (3) the loading rate of fluid injection pressure at the wellbore shown in Fig. 4 since the dynamic behavior of saturated porous media is significantly influenced by the fluid injection rate, which may come into play in the damage propagation. The analysis of dynamic coupling during wellbore fluid injection, taking into account the aforementioned factors, is directed at understanding hydraulic fracturing dynamics, which will be elaborated upon in the subsequent sections.

Damage–Permeability Coupling Behavior

In this section, we investigate the parameter that controls the coupling effects between damage and permeability in the saturated porous media subjected to fluid injection. Three simulation scenarios are tested by varying the damage–permeability coefficient b (i.e., $b = 0$, 14, and 16). From Eq. (13), the coupling intensity between damage and permeability increases with the value of b. When $b = 0$, the permeability is uncoupled with damage and remains unchanged during hydraulic simulations. In this case, the remaining processes such as fluid flow and coupled plasticity–damage failure are first confirmed. For the first scenario, we set fluid injection time $t_0 = 1.5$ ms and total loading time $t_1 = 2.5$ ms, and three initial permeabilities k_0 much greater than those given in Table 1 are chosen, which allows for simulation of more noticeable fluid flow and its effect on coupled plasticity–damage failure. The

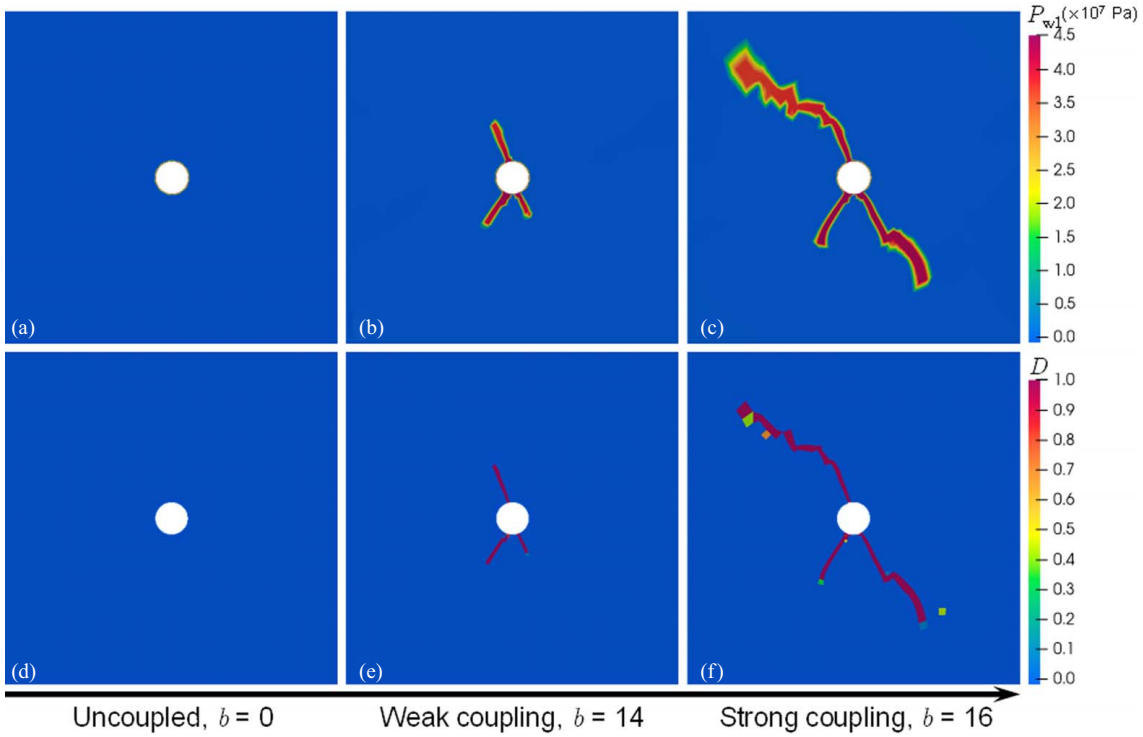

Fig. 6. Comparison of final results for near-wellbore rock formation across three damage–permeability coupling coefficients (i.e., $b = 0$, 14, and 16). The value of b determines the coupling intensity between damage and permeability. The uncoupled, weak coupling, and strong coupling scenarios are simulated. Examination of two responses after complete loading: (a–c) overpressure P_{w1}; and (d–f) damage D.

final results for near-wellbore rock formation across the three values of b are extracted and shown in Fig. 5. The pore-water overpressure P_{w1} decreases gradually from the inner wellbore boundary toward the outer domain boundaries, and the P_{w1} distribution along the radial direction agrees with the theoretical calculation, similar to that shown by Lisjak et al. (2017) and Yan et al. (2021). The increase of k_0 significantly accelerates the seepage flow in the matrix [Figs. 5(a–c)].

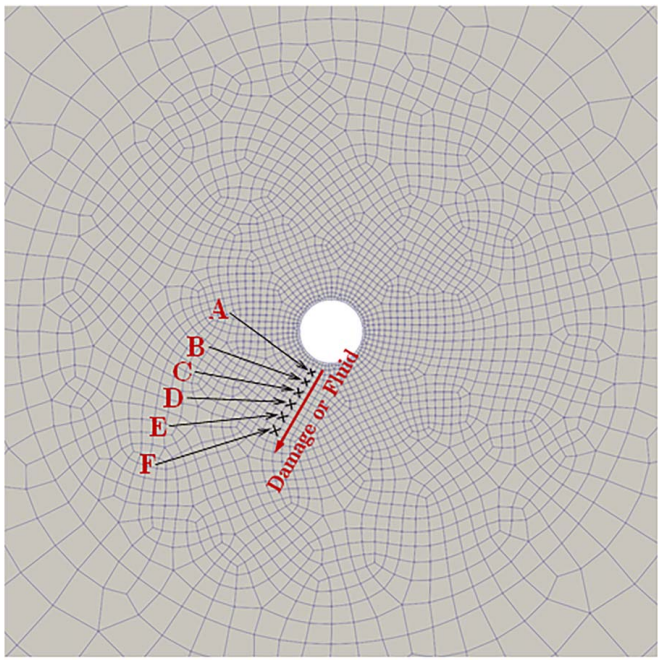

Fig. 7. Extracted elements within damage zones for the strong damage–permeability coupling scenario (i.e., $b = 16$). Six elements, namely, A, B, C, D, E, and F, are distributed along the direction of damage evolution or fluid flow.

The wellbore boundary is constantly pressurized by the injected fluid while the fluid flows in the rock matrix. During the loading, the rock near the wellbore first undergoes dynamic poroelastic deformation, then reaches mixed-mode failure including plastic shear and tensile damage. From Figs. 5(d–f), we observe two sets of conjugated zones (i.e., four localized plastic zones) developed near the wellbore. The plastic zones under shear are strengthened with increasing k_0, since the fluid flow promotes the diffusion of pore pressure p_w, which then raises the volumetric stress [i.e., $p_{n+1}^{\text{trial}} = -(K\varepsilon_{\text{vol}(n)} + p_{w(n)})$, where $\varepsilon_{\text{vol}(n)}$ denotes the volumetric strain] and further the plastic yield according to Eq. (7). Similarly, in comparison, the case with $k_0 = 1.0 \times 10^{-8}$ m^2 shows the largest range of tensile damage [Figs. 5(g–i)]. Note that the results clearly show no correlation between the permeability and damage since the damage-induced change (degradation) in antipermeability inevitably results in a preferential path of fluid flow instead of the linearized distribution of pore overpressure. This also aligns with expectations for the first simulation scenario where $b = 0$.

Fig. 6 compares the results of the three simulations considering different damage–permeability coupling intensities (i.e., $b = 0$, 14, and 16, representing the uncoupled, weak coupling, and strong coupling scenarios, respectively). The coupling between damage and permeability is considered in the simulations. For each simulation, we set a total loading time $t_1 = 25$ ms and initial permeability $k_0 = 2.0 \times 10^{-15}$ m^2, and all other parameters used are given in Table 1. In Figs. 6(a and d) ($b = 0$), the injected fluid pressure almost does not diffuse from the wellbore boundary (i.e., no fluid flow), and no tensile damage appears in the rock formation. This is different from the first scenario, demonstrating that the tensile damage that

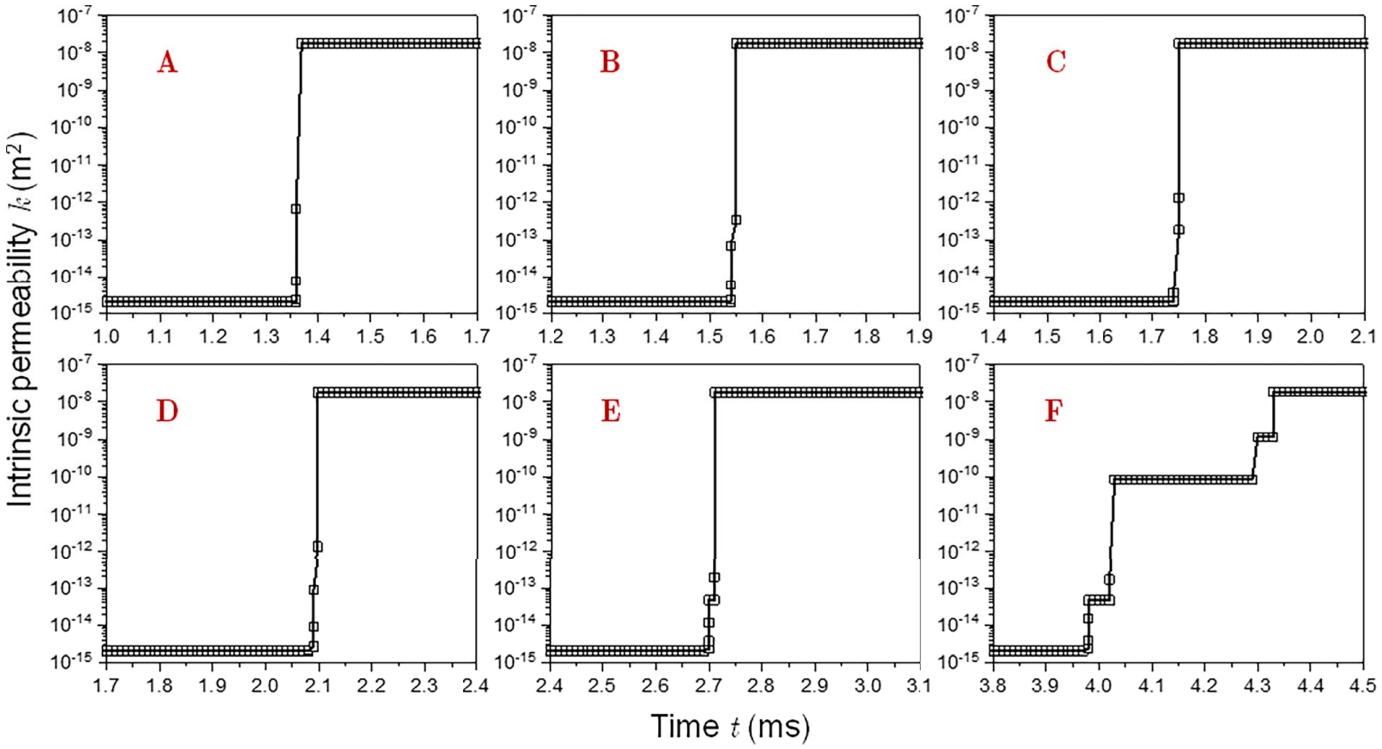

Fig. 8. Variations of intrinsic permeabilities k at the six focused elements (i.e., A, B, C, D, E, and F) with loading time t.

occurred in the first scenario is totally caused by the matrix seepage. However, in the damage–permeability coupling scenarios [Figs. 6(b, c, e, and f)], the apparent fluid flow paths (three narrow zones with higher overpressure) are formed near the wellbore and are almost consistent with that of tensile damage evolution. This is attributed to the coupling interaction between damage and permeability, wherein even slight degrees of tensile damage can result in significant degradation of rock's antipermeability [Eq. (13)], which sequentially facilitates the further propagation of tensile damage. As a result, the longest damage zone occurs in the strong damage–permeability coupling scenario. It is worth noting that the injected fluid cannot always flow into the lower-permeability zone induced by tensile damage due to the discontinuous damage zones, as shown in Figs. 6(c and f). Finally, fluid flow paths are generally divided into the intact rock matrix and the damage zones predominantly controlled by the damage–permeability coupling. The former allows for seepage, resulting in extremely limited damage due to the low permeability of actual rock formation; the latter is responsible for preferential flow during fluid injection, which dominates the drive of damage propagation.

To further investigate the damage–permeability coupling in Fig. 6, six elements (i.e., A, B, C, D, E, and F) within damage zones for the strong damage–permeability coupling scenario are extracted (Fig. 7), and the variations of intrinsic permeabilities at these elements with loading time are shown in Fig. 8. In the given scenario, the undamaged ($D = 0$) rock formation retains its initial intrinsic permeability (i.e., $k = k_0 = 2.0 \times 10^{-15}$ m^2), while the fully damaged ($D = 1$) rock formation experiences a reduction in intrinsic antipermeability k, with a value of 1.8×10^{-5} m^2, as determined by Eq. (13). Elastoplastic deformation smoothly transitions to damage propagation. The damage zone evolves from A to F with loading time, and so does the antipermeability degradation. The rate of antipermeability degradation also serves as a reflection of the propagation velocity of the damage zone during wellbore fluid injection. From Figs. 6 and 8, upon damage to the rock formulation in the vicinity of the wellbore (i.e., A), there is a rapid degradation in the antipermeability. The farthest element from the wellbore (i.e., F) experiences an antipermeability attenuation process of approximately 0.36 ms. This result arises from the decrease in fluid pore pressure as it flows from the wellbore to Element F. As a result, the diminished capacity to facilitate the continued propagation of damage leads to a slower degradation in antipermeability.

Damage Propagation Induced by Fluid Injection

We systematically analyzed the hydromechanical process during fluid injection for different in situ stress fields that may impact dynamic damage propagation. We chose $b = 16$ in the simulations for a more noticeable change in damage propagation owing to strong damage–permeability coupling. The wellbore injection simulations under three in situ stress fields (i.e., $\Delta\sigma = \sigma_H - \sigma_h| = 0$, 20, and 30 MPa) were performed. For each simulation, the damage and plasticity profiles at four loading time points (i.e., $t = 1.5$, 6.25, 12.5, and 25 ms) were extracted and are shown in Figs. 9 and 10. All the simulations show distinct variations in the length of damage zones, which reflect the spatial evolution or propagation of injection-induced damage over time (hydrofracturing). Meanwhile, the plastic zones under shear evolve from the wellbore boundary toward the outer domain boundaries (hydroshearing). The simultaneous capture of shear plasticity and tensile damage exhibits the mixed-mode fracture under fluid injection. The fracture trajectories controlled by tensile damage (Fig. 9) are almost covered with that controlled by shear plasticity (Fig. 10). The occurrence of shear plasticity precedes that of tensile damage in the simulation scenarios where the in situ stress field is anisotropic ($\Delta\sigma = 20$ or 30 MPa). In the isotropic in situ stress field scenario ($\Delta\sigma = 0$ MPa), however, damage and plasticity are almost simultaneously initiated at the wellbore circumference. The difference between the two observations reveals that the initial stress anisotropy hinders the initiation

of tensile damage to a certain extent, and the opposite is true for shear plasticity.

For the simulations under the three in situ stress fields, the damage and plasticity profiles show different evolution features, including orientation, magnitude, and trajectory, even at the same injection time. The orientation of damage evolution rotates clockwise from −11° ($\Delta\sigma = 0$ MPa) to −65° ($\Delta\sigma = 20$ MPa). Multiple fractures occur in the scenario with $\Delta\sigma = 30$ MPa, including −65° antiwing and −124° secondary fractures. Concerning the evolution magnitude at the same time, the damage for the scenario with $\Delta\sigma = 0$ MPa develops the most quickly, which finally forms the longest damage zones [Fig. 11(a)], whereas the plastic zones for the scenario with $\Delta\sigma = 20$ MPa are the shortest [Fig. 11(b)]. The spatial evolution of plastic and damaged points over time is shown in Fig. 11. Note that the plastic and damage states at each point are instantaneously determined in the simulations. The observed persistent damage at one point reflects the dynamic evolution of damage (D) from 0 (undamaged) to 1 (fully damaged). The tensile components of stresses at the damaged points are reduced even to zero, which keeps changing the stress states under

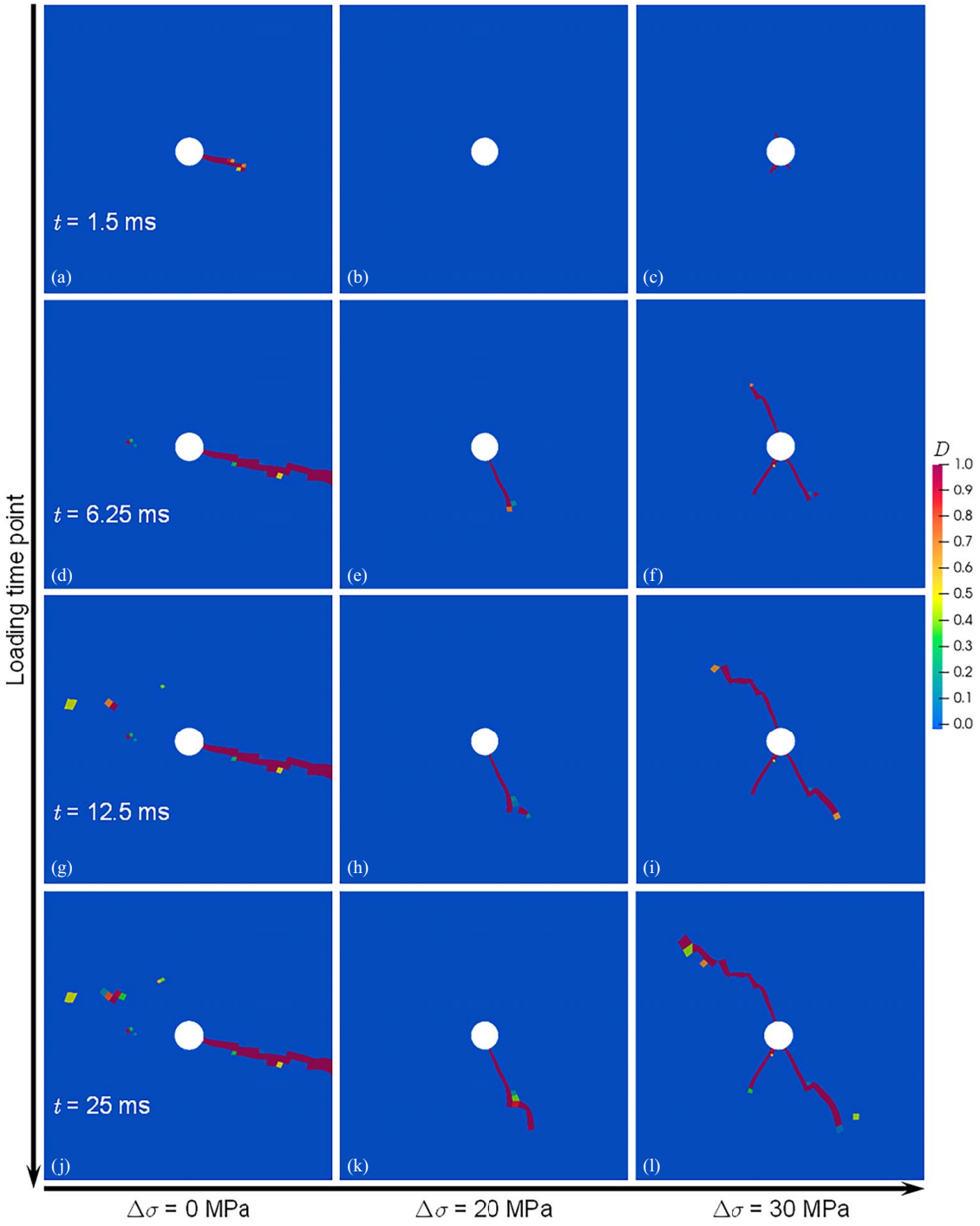

Fig. 9. Evolution of fluid injection-induced damage in the rock formation under different in situ stress fields. Three stress differences between the maximum (σ_H) and minimum (σ_h) horizontal stresses are chosen, i.e., $\Delta\sigma = 0$, 20, and 30 MPa. Damage profiles extracted at four loading time points: (a–c) $t = 1.5$ ms; (d–f) $t = 6.25$ ms; (g–i) $t = 12.5$ ms; and (j–l) $t = 25$ ms.

wellbore fluid pressure. At the later loading stage for the scenario with $\Delta\sigma = 0$ or 20 MPa [Fig. 11(a)], we observed relatively sparse damaged points, indicating that the continued damage propagation tends to slow down over time. The scenario with $\Delta\sigma = 30$ MPa is not the case, for which the damage propagation is expected to proceed over time.

Fluid injection may induce seismicity due to stress drop occurring with damage and plasticity that sometimes has unexpectedly large earthquake magnitudes (Ellsworth 2013; Lyakhovsky and Shalev 2021). Seismic events during fluid injection are supposed to be recorded and measured to predict seismic hazards (Li et al. 2023a). We employed the determination equation suggested by Hanks and Kanamori (1979), where the moment magnitude M_w is proportional to the logarithm of the potency P_0 [i.e., $M_w = 2\log(\mu \times P_0)/3 - 6.0$, $\mu = 30$ GPa]. Potency corresponds to the product of equivalent plastic shear strain and element volume. Fig. 12 compares the temporal evolution of cumulated potency and moment magnitude for the three in situ stress fields. By comparison, the maximum potency is cumulated in the scenario with $\Delta\sigma = 0$ MPa because the longest fracture affects the largest zones. The variation trends at the later stage of loading observed in Fig. 12(a) confirm the change of damaged points shown in Fig. 11(a). For the scenario with $\Delta\sigma = 0$ MPa, the moment magnitude reaches the maximum (i.e., $M_w = 0.044$) at $t = 25$ ms [Fig. 11(b)]. Note that $M_w < -3$ corresponds to extremely small magnitudes, and the event with $M_w \geq 1$ is referred to as a strong

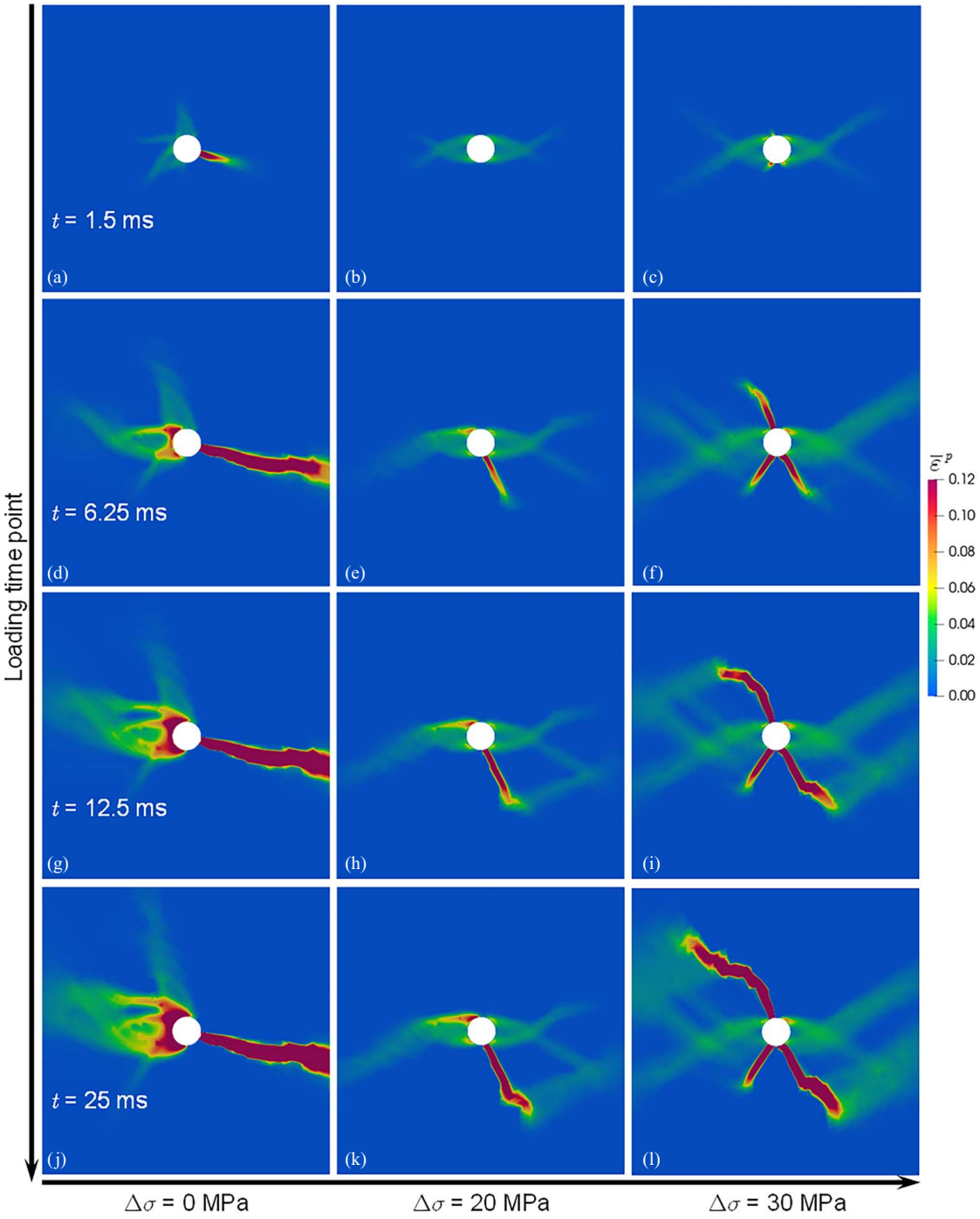

Fig. 10. Distribution and evolution of plasticity during wellbore fluid injection in the rock formation under different in situ stress fields.

Int. J. Geomech., 2025, 25(4): 04025019

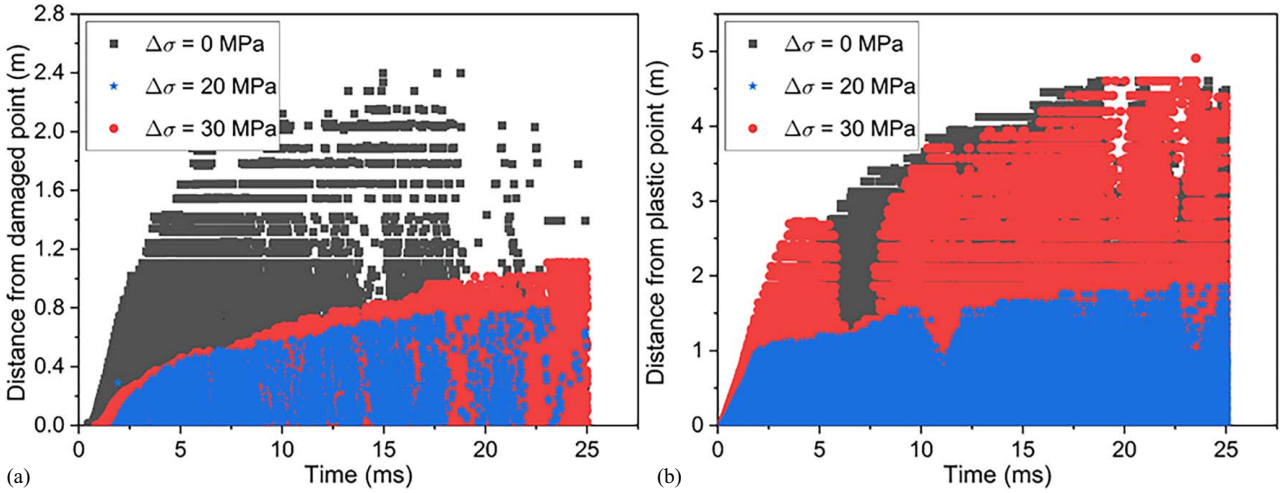

Fig. 11. Spatial evolution of (a) plastic; and (b) damaged points over time for different in situ stress fields. The y-axis represents the distance from the wellbore circumference to the point with stress drop resulting from plastic or damage.

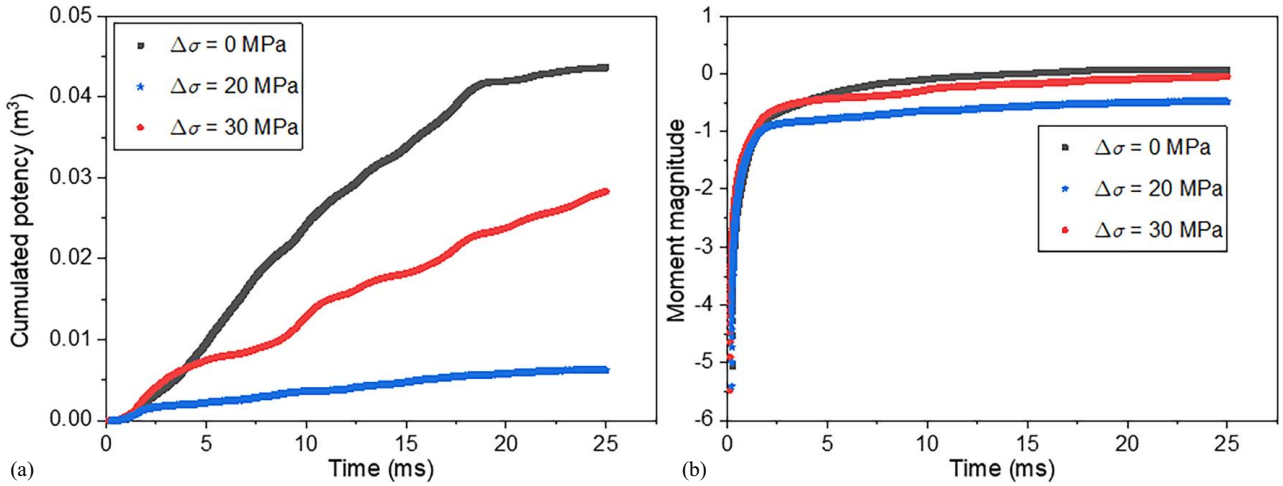

Fig. 12. Temporal evolution of (a) cumulated potency; and (b) moment magnitude for different in situ stress fields. Seismic events induced by fluid injection are recorded.

seismic event (Lyakhovsky and Shalev 2021). The induced event with maximum moment magnitude in the scenario with $\Delta\sigma =$ 0 MPa thus fails to reach strong seismicity.

Role of Fluid Loading Rate in Dynamic Damage Propagation

In this section, we explore the role of fluid loading rate in damage propagation induced by fluid injection that significantly influences dynamic coupling between plasticity–damage and permeability. We performed three hydraulic simulations by varying the fluid injection time (i.e., $t_0 = 1.5$, 2.5, and 10 ms) while maintaining the total loading time $t_1 = 25$ ms. The injected fluid pressure was linearly imposed within the times above (t_0), resulting in three fluid loading rates. Fig. 13 compares the simulation results at two loading end-time points for different fluid loading rates. Comparing the fluid overpressure profiles at the end of wellbore injection ($t = t_0$) and total loading ($t = t_1$), we see that the distance of damage propagation at the stage of fluid injection [Figs. 13(a–c)] is much smaller than that at the subsequent loading stage (constant injection pressure) [Figs. 13(d–f)]. This significant variation suggests that the dynamics induced after injection furthers the damage evolution (dynamic hydraulic fracturing) and dominates the damage propagation course in the entire loading. Its acquisition can be attributed to the dynamics solution of porous media using the explicit predictor–corrector scheme for the dynamic hydromechanical coupled problems in this study. The oscillations observed in the temporal–spatial evolution curves of damaged and plastic points (Fig. 14), cumulated potency, and moment magnitude (Fig. 15) also confirm the occurred fracturing dynamics.

For the simulations under three injection rates, the fluid overpressure profiles show different distances of fluid flow coupled with damage in saturated porous media (Fig. 13). At the end of wellbore fluid injection, the distance of damage zones (almost consistent with that of fluid flow) enhances with increasing t_0. However, the longest distance of damage propagation occurs in the scenario with the least fluid injection time (i.e., $t_0 = 1.5$ ms) at the end of the same total loading time t_1. This significant difference arises from the stronger dynamics being excited in a shorter wellbore injection time, leading to greater propagation of damage. On the other hand, the number and orientations of induced fractures are not affected by the fluid loading rate, as shown in Fig. 13.

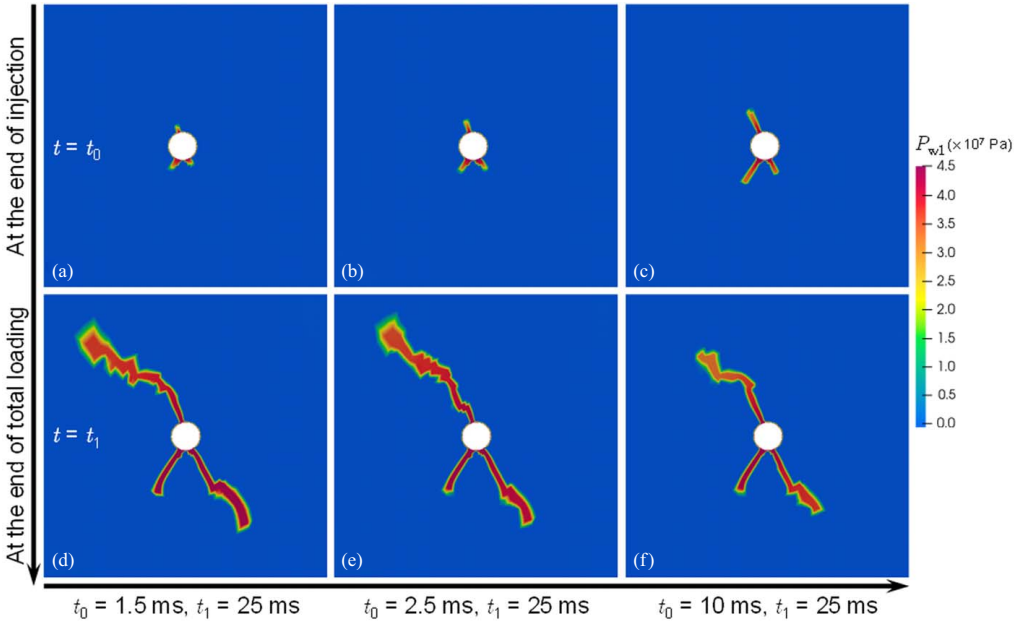

Fig. 13. Comparison between simulation results at two loading end-time points for different times of fluid injection (i.e., $t_0 = 1.5$, 2.5, and 10 ms). The total loading times in the simulations are the same ($t_1 = 20$ ms). Evolution of fluid overpressure during loading: (a–c) at the end of wellbore injection ($t = t_0$); and (d–f) at the end of total loading ($t = t_1$).

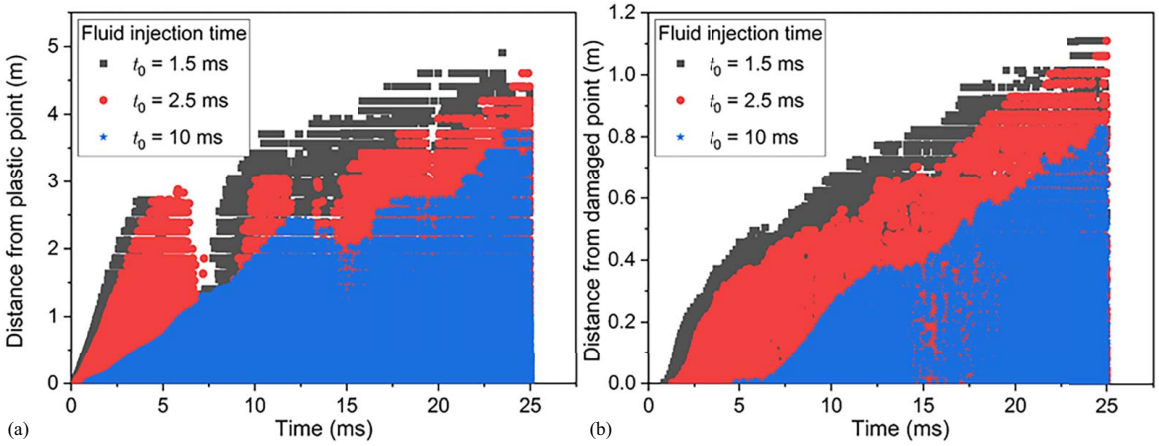

Fig. 14. Spatial evolution of (a) damaged; and (b) plastic points over time for different times of fluid injection.

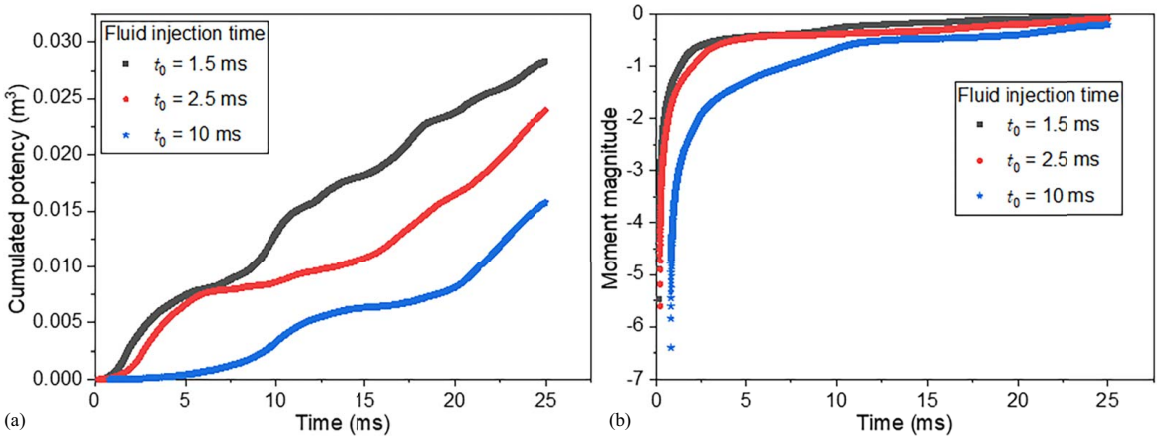

Fig. 15. Temporal evolution of (a) cumulated potency; and (b) moment magnitude for different times of fluid injection.

The temporal–spatial evolution results shown in Figs. 14 and 15 provide novel insights toward a better understanding of the nucleation and propagation of damage, plasticity, and seismicity induced by fluid injection. In the early stage of loading, the increase of fluid injection rate speeds up the occurrences of plastic and damaged points and the enhancement of cumulated potency and moment magnitude. From Fig. 15(a), the amplitude of the oscillations in the evolution of cumulated potency gradually decreases with time, which exhibits the release of energy accumulated in a short fluid injection time. Furthermore, the period of oscillation increases with the fluid injection time t_0. In all simulations [Fig. 15(b)], the maximum moment magnitude M_w reaches 0.028 (at $t = 25$ ms in the scenario with $t_0 = 1.5$ ms). The corresponding event during fluid injection is also out of reach in strong seismicity. All told, the previous observations suggest that the propagation of damage, plasticity, and seismicity is controlled by fracturing dynamics induced by fluid injection.

Conclusions

The integration of dynamic Biot's poroelasticity with coupled Drucker–Prager plasticity, Grady–Kipp damage, and antipermeability degradation is performed to simulate the effects of dynamic hydraulic fracturing caused by fluid injection. We smoothly obtain the dynamics solution of saturated porous media by employing an explicit predictor–corrector scheme, which can be used to identify the key factors controlling dynamic damage propagation. The examination of the proposed model in soil column consolidation and rock hydraulic fracturing driven by a pre-existing crack demonstrates good agreement between the numerical simulations and experimental observations. The intact rock allows for seepage, leading to extremely limited damage owing to the low permeability of actual rock formation. The damage zones are responsible for preferential flow during fluid injection due to damage-induced degradation. During the loading, the plastic zones under shear (hydroshearing) and the damage zones under tensile (hydrofracturing) evolve from the wellbore boundary toward the outer domain boundaries. In this process, elastoplastic deformation smoothly transitions to damage propagation. The simultaneous capture of plasticity and damage exhibits the mixed shear and tensile fractures under fluid injection. The longest damage zone occurs in the strong damage–permeability coupling scenario. The initial stress anisotropy hinders the initiation of tensile damage to a certain extent, and the opposite is true for shear plasticity.

The distance of damage propagation at the end of the fluid injection stage is much smaller than that at the end of the total loading stage, owing to the fact that the energy accumulated by wellbore injection cannot be released quickly. However, the fluid loading rate does not affect the number and orientations of induced fractures. The injection-induced dynamics further the damage after injection and dominate the damage propagation course in the entire loading. The fracturing dynamics induced by fluid injection are confirmed by the oscillations observed in the temporal–spatial evolution curves of damaged and plastic points, cumulated potency, and moment magnitude. The stronger dynamics are excited in a shorter injection time, leading to more significant damage propagation. Two main features of fracturing dynamics are as follows: (1) the period of oscillations in the evolution of cumulated potency increases with the fluid injection time, and (2) the amplitude of the oscillations gradually decreases with time due to energy release. The propagation of shear plasticity, tensile damage, and induced seismicity is dominated by fracturing dynamics induced by fluid injection.

While our model effectively simulates dynamic hydraulic fracturing induced by fluid injection, acknowledging its limitations is essential for enhancement. It assumes isotropic material properties, potentially neglecting the intricate anisotropic characteristics of actual rock formations. Moreover, it may not fully account for all complexities of rock–fluid interactions, such as chemical reactions or heterogeneous rock properties. Investigating the long-term effects of fluid injection on reservoir behavior remains a critical area for further exploration.

Data Availability Statement

Some or all data, models, or codes that support the findings of this study are available from the corresponding author upon reasonable request.

Acknowledgments

This work is supported by the Guangdong Basic and Applied Basic Research Foundation (2023A1515110593), the Shenzhen Science and Technology Program (JCYJ20220530113612028), and the Guangdong Provincial Key Laboratory of Geophysical High-resolution Imaging Technology (2022B1212010002).

Notation

The following symbols are used in this paper:

$\mathbf{B}$ = shape function gradient matrix;
b = damage–permeability coupling coefficient;
$\mathbf{b}$ = left Cauchy–Green strain;
$\mathbf{C}$ = damping matrix;
c = cohesion;
D = damage parameter;
E = Young's modulus;
$\mathbf{F}$ = deformation gradient;
$\mathbf{f}^{\text{ext}}$ = external force;
G = shear modulus;
$\mathbf{g}$ = gravity acceleration;
H = generalized hardening modulus;
$h_{\min}$ = minimum mesh size;
K = bulk modulus;
k = intrinsic permeability;
$\mathbf{k}$ = permeability vector;
k^{rw} = water relative permeability coefficient;
$\mathbf{M}$ = lumped mass matrix;
M_w = moment magnitude.;
$\mathbf{m}$ = identity matrix in Voigt notation;
$\dot{m}_e$ = mass rate of water lost through evaporation per unit volume;
m_{wb}, k_{wb}, α_{wb} = Weibull's parameters;
$\mathbf{N}$ = shape function matrix;
N^{ϵ} = softening exponent;
$\mathbf{n}$ = normal vector on applied boundary surface;
n = porosity;
n_{nd}, n_{gp} = number of nodes and Guass points;
P_0 = potency;
P_{w0} = initial pore-water pressure;
$P_{w1}^{\text{Injection}}$ = injected fluid overpressure;
Q = volumetric compressibility of mixture;
p = pressure;
$\mathbf{R}$ = internal force vector;

S = saturation;
$\mathbf{s}$ = deviatoric stress tensor;
T = temperature;
t = time;
$\mathbf{U}$ = displacement of fluid;
$\mathbf{u}$ = displacement of solid;
V_{gp} = volume of Gauss point;
$\mathbf{v}$ = velocity;
v_c = P-wave velocity;
$\mathbf{w}$ = relative displacement of fluid with respect to solid;
$\mathbf{x}$ = node position;
α = Biot's coefficient;
α_F, α_Q, β_C = constitutive parameters;
β_s, β_w, β_{mt} = thermal expansion coefficients of solid, fluid, and mixture;
γ_N, β_N, θ_N = Newmark parameters;
$\Delta\gamma$ = plastic multiplier;
$\boldsymbol{\varepsilon}$ = strain tensor;
$\bar{\varepsilon}$ = equivalent strain;
κ = hydraulic conductivity;
λ, μ = Lamé constants;
μ_w = dynamic viscosity of water;
ν = Poisson's ratio;
ρ = density;
$\boldsymbol{\sigma}$ = stress tensor;
$\boldsymbol{\sigma}'$ = effective stress tensor;
$\tilde{\sigma}$ = principal stress;
σ_H, σ_h, σ_v = maximum horizontal, minimum horizontal, and vertical stresses from in situ stress field;
ϕ = internal friction angle;
Φ = yield function; and
ψ = dilatancy angle.

References

AbuAisha, M., B. Loret, and D. Eaton. 2016. "Enhanced geothermal systems (EGS): Hydraulic fracturing in a thermo-poroelastic framework." *J. Pet. Sci. Eng.* 146: 1179–1191. https://doi.org/10.1016/j.petrol.2016.07.027.

Ai, S. G., and K. Gao. 2023. "Elastoplastic damage modeling of rock spalling/failure induced by a filled flaw using the material point method (MPM)." *Rock Mech. Rock Eng.* 56: 4133–4151. https://doi.org/10.1007/s00603-023-03265-8.

Camacho, G. T., and M. Ortiz. 1997. "Adaptive Lagrangian modelling of ballistic penetration of metallic targets." *Comput. Methods Appl. Mech. Eng.* 142 (3–4): 269–301. https://doi.org/10.1016/S0045-7825(96)01134-6.

Cao, T. D., F. Hussain, and B. A. Schrefler. 2018. "Porous media fracturing dynamics: Stepwise crack advancement and fluid pressure oscillations." *J. Mech. Phys. Solids* 111: 113–133. https://doi.org/10.1016/j.jmps.2017.10.014.

Chan, A. H., M. Pastor, B. A. Schrefler, T. Shiomi, and O. C. Zienkiewicz. 2022. *Computational geomechanics: Theory and applications*. Hoboken, NJ: Wiley.

Chen, B., B. R. Barboza, Y. Sun, J. Bai, H. R. Thomas, M. Dutko, M. Cottrell, and C. Li. 2021. "A review of hydraulic fracturing simulation." *Arch. Comput. Methods Eng.* 29: 1–58. https://doi.org/10.1007/s11831-021-09653-z.

Chen, E. P. 1999. "Non-local effects on dynamic damage accumulation in brittle solids." *Int. J. Numer. Anal. Methods Geomech.* 23 (1): 1–21. https://doi.org/10.1002/(SICI)1096-9853(199901)23:1<1::AID-NAG892>3.0.CO;2-R.

Chen, Z., and L. Shen. 2021. "A modified smoothed particle hydrodynamics for modelling fluid-fracture interaction at mesoscale." *Comput. Part. Mech.* 9: 277–297. https://doi.org/10.1007/s40571-021-00409-x.

Cheng, L., Z. Luo, L. Zhao, and Y. Xie. 2022. "Numerical analysis of fracture deformation and instability during CO_2 geological sequestration using a THM-XFEM coupled model." *Comput. Geotech.* 145: 104664. https://doi.org/10.1016/j.compgeo.2022.104664.

Das, R., and P. W. Cleary. 2010. "Effect of rock shapes on brittle fracture using smoothed particle hydrodynamics." *Theor. Appl. Fract. Mech.* 53 (1): 47–60. https://doi.org/10.1016/j.tafmec.2009.12.004.

Douillet-Grellier, T., B. D. Jones, R. Pramanik, K. Pan, A. Albaiz, and J. R. Williams. 2016. "Mixed-mode fracture modeling with smoothed particle hydrodynamics." *Comput. Geotech.* 79: 73–85. https://doi.org/10.1016/j.compgeo.2016.06.002.

Ellsworth, W. L. 2013. "Injection-induced earthquakes." *Science* 341 (6142): 1225942. https://doi.org/10.1126/science.1225942.

Grady, D. E., and M. E. Kipp. 1980. "Continuum modelling of explosive fracture in oil shale." *Int. J. Rock Mech. Min. Sci. Geomech. Abstr.* 17: 147–157. https://doi.org/10.1016/0148-9062(80)91361-3.

Guo, P., M. Wang, G. Dang, T. Zhu, J. Wang, and M. He. 2023. "Evaluation method of underground water storage space and thermal reservoir model in abandoned mine." *Rock Mech. Bull.* 2 (2): 100044. https://doi.org/10.1016/j.rockmb.2023.100044.

Hanks, T. C., and H. Kanamori. 1979. "A moment magnitude scale." *J. Geophys. Res.: Solid Earth* 84 (B5): 2348–2350. https://doi.org/10.1029/JB084iB05p02348.

Keilegavlen, E., L. Duboeuf, A. M. Dichiarante, S. Halldórsdóttir, I. Stefansson, M. Naumann, E. Á. Guðnason, K. Ágústsson, G. H. Eggertsson, and V. Oye. 2021. "Hydro-mechanical simulation and analysis of induced seismicity for a hydraulic stimulation test at the Reykjanes geothermal field, Iceland." *Geothermics* 97: 102223. https://doi.org/10.1016/j.geothermics.2021.102223.

Kruszewski, M., et al. 2021. "Integrated stress field estimation and implications for enhanced geothermal system development in Acoculco, Mexico." *Geothermics* 89: 101931. https://doi.org/10.1016/j.geothermics.2020.101931.

Lepillier, B., K. Yoshioka, F. Parisio, R. Bakker, and D. Bruhn. 2020. "Variational phase-field modeling of hydraulic fracture interaction with natural fractures and application to enhanced geothermal systems." *J. Geophys. Res.: Solid Earth* 125 (7): e2020JB019856. https://doi.org/10.1029/2020JB019856.

Lewis, R. W., and B. Schrefler. 1998. *The finite element method in the static and dynamic deformation and consolidation of porous media*. Hoboken, NJ: Wiley.

Li, C., R. I. Borja, and R. A. Regueiro. 2004. "Dynamics of porous media at finite strain." *Comput. Methods Appl. Mech. Eng.* 193 (36–38): 3837–3870. https://doi.org/10.1016/j.cma.2004.02.014.

Li, S., Q. Wu, L. Wang, H. Luo, C. Li, X. Huo, Y. Liu, and D. Wang. 2023a. "Seismic behavior analysis of soft and hard interbedded rock slope considering vibration deterioration of discontinuities at the interface between different rock types in meizoseismal area—A case study." *Bull. Eng. Geol. Environ.* 82 (1): 14. https://doi.org/10.1007/s10064-022-03036-9.

Li, Z., X. Ma, X.-Z. Kong, M. O. Saar, and D. Vogler. 2023b. "Permeability evolution during pressure-controlled shear slip in saw-cut and natural granite fractures." *Rock Mech. Bull.* 2 (2): 100027. https://doi.org/10.1016/j.rockmb.2022.100027.

Liao, S., J. Hu, and Y. Zhang. 2024. "Mechanism of hydraulic fracture vertical propagation in deep shale formation based on elastic–plastic model." *Eng. Fract. Mech.* 295: 109806. https://doi.org/10.1016/j.engfracmech.2023.109806.

Lisjak, A., P. Kaifosh, L. He, B. S. A. Tatone, O. K. Mahabadi, and G. Grasselli. 2017. "A 2D, fully-coupled, hydro-mechanical, FDEM formulation for modelling fracturing processes in discontinuous, porous rock masses." *Comput. Geotech.* 81: 1–18. https://doi.org/10.1016/j.compgeo.2016.07.009.

Liu, D., Z. Shen, L. Xu, L. Gan, and G. Li. 2018. Vol. 16 of *Experimental study on critical internal water pressure of hydraulic fracturing of fractured rock mass*, 140–145. Beijing: South-to-North Water Transfers and Water Science & Technology.

Liu, X. 1994. "On the stability of a Newmark's scheme-based predictor-corrector algorithm." *Comput. Struct.* 53 (1): 27–33. https://doi.org/10.1016/0045-7949(94)90126-0.

Lyakhovsky, V., Y. Ben-Zion, and A. Agnon. 1997. "Distributed damage, faulting, and friction." *J. Geophys. Res.: Solid Earth* 102 (B12): 27635–27649. https://doi.org/10.1029/97JB01896.

Lyakhovsky, V., and E. Shalev. 2021. "Runaway versus stable fracturing during hydraulic stimulation: Insights from the damage rheology modeling." *Rock Mech. Rock Eng.* 54: 5449–5464. https://doi.org/10.1007/s00603-021-02395-1.

Maeda, Y., S. Ogata, D. Fukuda, H. Liu, and T. Inui. 2024. "Development of a GPGPU-parallelized FDEM based on extrinsic cohesive zone model with master-slave algorithm." *Comput. Geotech.* 166: 105942. https://doi.org/10.1016/j.compgeo.2023.105942.

Navas, P., M. Molinos, M. M. Stickle, D. Manzanal, A. Yagüe, and M. Pastor. 2022. "Explicit meshfree u-pw solution of the dynamic Biot formulation at large strain." *Comput. Part. Mech.* 9 (4): 655–671. https://doi.org/10.1007/s40571-021-00436-8.

Pan, K., R. Pramanik, B. D. Jones, T. Douillet-Grellier, A. Albaiz, and J. R. Williams. 2016. "Development of fluid-solid coupling for the study of hydraulic fracturing using SPH." In *Proc., 11 Int. SPHERIC Workshop, TUM*, 47–54. Munich, Germany: Technical University of Munich.

Papoulia, K. D., C.-H. Sam, and S. A. Vavasis. 2003. "Time continuity in cohesive finite element modeling." *Int. J. Numer. Methods Eng.* 58 (5): 679–701. https://doi.org/10.1002/nme.778.

Parchei-Esfahani, M., B. Gee, and R. Gracie. 2020. "Dynamic hydraulic stimulation and fracturing from a wellbore using pressure pulsing." *Eng. Fract. Mech.* 235: 107152. https://doi.org/10.1016/j.engfracmech.2020.107152.

Parchei-Esfahani, M., and R. Gracie. 2019. "On the undrained and drained hydraulic fracture splits." *Int. J. Numer. Methods Eng.* 118 (12): 741–763. https://doi.org/10.1002/nme.6036.

Peruzzo, C., D. T. Cao, E. Milanese, P. Favia, F. Pesavento, F. Hussain, and B. A. Schrefler. 2019. "Dynamics of fracturing saturated porous media and self-organization of rupture." *Eur. J. Mech. A. Solids* 74: 471–484. https://doi.org/10.1016/j.euromechsol.2018.12.004.

Picandet, V., A. Khelidj, and G. Bastian. 2001. "Effect of axial compressive damage on gas permeability of ordinary and high-performance concrete." *Cem. Concr. Res.* 31 (11): 1525–1532. https://doi.org/10.1016/S0008-8846(01)00546-4.

Pizzocolo, F., J. M. Huyghe, and K. Ito. 2013. "Mode I crack propagation in hydrogels is step wise." *Eng. Fract. Mech.* 97: 72–79. https://doi.org/10.1016/j.engfracmech.2012.10.018.

Pramanik, R., and D. Deb. 2015. "Implementation of smoothed particle hydrodynamics for detonation of explosive with application to rock fragmentation." *Rock Mech. Rock Eng.* 48: 1683–1698. https://doi.org/10.1007/s00603-014-0657-y.

Rahimi-Aghdam, S., V.-T. Chau, H. Lee, H. Nguyen, W. Li, S. Karra, E. Rougier, H. Viswanathan, G. Srinivasan, and Z. P. Bažant. 2019. "Branching of hydraulic cracks enabling permeability of gas or oil shale with closed natural fractures." *Proc. Natl. Acad. Sci. USA* 116 (5): 1532–1537. https://doi.org/10.1073/pnas.1818529116.

Raymond, S. J., B. D. Jones, and J. R. Williams. 2019. "Modeling damage and plasticity in aggregates with the material point method (MPM)." *Comput. Part. Mech.* 6 (3): 371–382. https://doi.org/10.1007/s40571-018-00218-9.

Raymond, S. J., B. D. Jones, and J. R. Williams. 2021. "Fracture shearing of polycrystalline material simulations using the material point method." *Comput. Part. Mech.* 8 (2): 259–272. https://doi.org/10.1007/s40571-020-00327-4.

Raziperchikolaee, S., V. Alvarado, and S. Yin. 2013. "Effect of hydraulic fracturing on long-term storage of CO_2 in stimulated saline aquifers." *Appl. Energy* 102: 1091–1104. https://doi.org/10.1016/j.apenergy.2012.06.043.

Sabetamal, H., M. Nazem, S. W. Sloan, and J. P. Carter. 2016. "Frictionless contact formulation for dynamic analysis of nonlinear saturated porous media based on the mortar method." *Int. J. Numer. Anal. Methods Geomech.* 40 (1): 25–61. https://doi.org/10.1002/nag.2386.

Sanavia, L., F. Pesavento, and B. A. Schrefler. 2006. "Finite element analysis of non-isothermal multiphase geomaterials with application to strain localization simulation." *Comput. Mech.* 37 (4): 331–348. https://doi.org/10.1007/s00466-005-0673-6.

Shalev, E., and V. Lyakhovsky. 2013. "The processes controlling damage zone propagation induced by wellbore fluid injection." *Geophys. J. Int.* 193 (1): 209–219. https://doi.org/10.1093/gji/ggt002.

Souley, M., F. Homand, S. Pepa, and D. Hoxha. 2001. "Damage-induced permeability changes in granite: A case example at the URL in Canada." *Int. J. Rock Mech. Min. Sci.* 38 (2): 297–310. https://doi.org/10.1016/S1365-1609(01)00002-8.

Suzuki, K., M. Oda, M. Yamazaki, and T. Kuwahara. 1998. "Permeability changes in granite with crack growth during immersion in hot water." *Int. J. Rock Mech. Min. Sci.* 35 (7): 907–921. https://doi.org/10.1016/S0148-9062(98)00016-3.

Tang, C. A., L. G. Tham, P. K. K. Lee, T. H. Yang, and L. C. Li. 2002. "Coupled analysis of flow, stress and damage (FSD) in rock failure." *Int. J. Rock Mech. Min. Sci.* 39 (4): 477–489. https://doi.org/10.1016/S1365-1609(02)00023-0.

Wang, S. Y., L. Sun, A. S. K. Au, T. H. Yang, and C. A. Tang. 2009. "2D-numerical analysis of hydraulic fracturing in heterogeneous geomaterials." *Constr. Build. Mater.* 23 (6): 2196–2206. https://doi.org/10.1016/j.conbuildmat.2008.12.004.

Wu, D., H. Li, D. Fukuda, and H. Liu. 2023. "Development of a finite-discrete element method with finite-strain elasto-plasticity and cohesive zone models for simulating the dynamic fracture of rocks." *Comput. Geotech.* 156: 105271. https://doi.org/10.1016/j.compgeo.2023.105271.

Yan, C., H. Fan, D. Huang, and G. Wang. 2021. "A 2D mixed fracture–pore seepage model and hydromechanical coupling for fractured porous media." *Acta Geotech.* 16 (10): 3061–3086. https://doi.org/10.1007/s11440-021-01183-z.

Zhang, B.-n., B. Han, and Q. Zhang. 2024. "An improved GPU-parallelized 2D/3D elastoplastic-damage-fracture joint framework for combined finite–discrete-element program." *Rock Mech. Rock Eng.*. 57: 3971–3991. https://doi.org/10.1007/s00603-023-03738-w.

Zhao, X., and R. P. Young. 2011. "Numerical modeling of seismicity induced by fluid injection in naturally fractured reservoirs." *Geophysics* 76 (6): WC167–WC180. https://doi.org/10.1190/geo2011-0025.1.